



Hydro- and aero-elastic response of floating offshore wind turbines to combined waves and wind in frequency domain

Azin Lamei¹ · Masoud Hayatdavoodi^{1,2} · H. Ronald Riggs³

Received: 25 October 2022 / Accepted: 9 February 2024 / Published online: 16 March 2024
© The Author(s) 2024

Abstract

An analytical approach and numerical solution to determine coupled aeroelastic and hydroelastic response of floating offshore wind turbines of arbitrary shape to combined wind and wave loads is presented. The model considers simultaneously the aerodynamic and hydrodynamic loads on an FOWT and integrates these with finite element method for structural analysis due to the combined loads. The hydrodynamic and aerodynamic loads are determined based on the linear wave diffraction theory and steady blade element momentum method, respectively, and the solution is obtained in frequency domain. The structure may be fixed or floating, located in arbitrary water depth, and may host single or multiple wind towers. The model captures the complete translational and rotational motions of the body in three dimensions, and the elasticity of the blades, tower and the floating platform. To assess the performance of the model, rigid and elastic responses of a FOWT to combined wave and wind loads are computed and compared with available laboratory measurements and other theoretical approaches where possible, and overall very good agreement is observed. The model developed in this study addresses directly three shortcomings of existing approaches used for the analysis of FOWTs, namely (i) determination of the elastic responses of the entire structure including the floating platform, (ii) analysis of the motion and elastic response of FOWTs in frequency domain, and (iii) assessment of responses of FOWTs with single or multiple wind towers.

Keywords Floating offshore wind turbines · Hydroelasticity · Aeroelasticity · Wave-wind loads

1 Introduction

Wind energy is a promising type of renewable energy. In year 2022, with 77.6 GW new installations of wind turbines, the global cumulative wind power capacity is 906 GW (Lee and Zhao 2023) with 68.8 GW and 8.8 GW wind power growth in onshore and offshore wind, respectively. Offshore wind turbines usually benefit from steadier and stronger wind fields than are present onshore. By the end of 2022, 64.3 GW offshore wind capacity was installed, which is 7% of global wind turbine installations; see Lee and Zhao (2023). While bottom-mounted offshore wind turbines are limited to nearshore sites

and shallow waters, floating offshore wind turbines allow for selection of sites farther offshore, in deeper waters, where the wind is stronger. With 80% of the world's offshore wind resource potential in waters with more than 60 m depth, interest in floating offshore wind turbines (FOWTs) is growing. By the end of 2022, a total of 171 MW floating wind was installed globally, with about 91% of its global installation in Europe (Lee and Zhao 2023).

Based on the knowledge and experience obtained from existing technologies of fixed onshore and nearshore wind turbines, and offshore floating platforms of the oil and gas platforms. Various concepts of floating platforms have been tested and developed for FOWTs, namely SPARs, semi-submersibles, barges and TLPs; see e.g. Govindji et al. (2014) and Uzunoglu et al. (2016) for more details.

On the other hand, the installation of a wind turbine on a floating platform introduces significant engineering challenges. FOWTs are subject to combined wind, waves and current loads. Predicting their dynamic response to the environmental loads is challenging for the state of the art. Motions of a FOWT result from the simultaneous effect of aerody-

✉ Masoud Hayatdavoodi
mhayatdavoodi@dundee.ac.uk

¹ Civil Engineering Department, School of Science and Engineering, University of Dundee, Dundee DD1 4HN, UK

² College of Shipbuilding Engineering, Harbin Engineering University, Harbin 150001, China

³ Civil and Environmental Engineering Department, University of Hawaii, Honolulu, HI 96822, USA

dynamic load on the rotor and the tower, hydrodynamic load of waves and current on the platform, and the restoring mooring forces. If elastic deformations of the structure to the aerodynamic and hydrodynamic loads are significant, it is crucial to also consider the elastic responses.

The aero-hydro-servo-elastic coupling numerical tools can be classified into two main groups: fully-coupled numerical tools and decoupled numerical tools. The former approach solves the governing equations of the fluid, the structure and the mooring lines simultaneously with no assumption about the magnitude of the motions, whereas in the latter approach the hydrodynamic and aerodynamic loads and responses are decoupled and often subject to simplifying assumptions about the magnitude of the motions. Figure 1 summarises the numerical approaches that are commonly applied for structural analysis, hydrodynamic and aerodynamic loads and responses. While providing a higher level of details and subject to fewer assumptions, fully coupled approaches are computationally very demanding and less practical. In fully-coupled numerical tools, to reduce the computational effort it is common to simplify the problem by restricting the motion and limit the elasticity analysis of the structure (if considered) to only the wind turbine, see e.g. Liu et al. (2017) and Bruinsma et al. (2018). Decoupled numerical approaches offer more efficient simulations but assume that the motions are small, see Salehyar et al. (2017) and Leimeister et al. (2020) among others. Reviews on existing numerical coupling tools for FOWTs are presented in e.g. Matha et al. (2011), Cruz and Atcheson (2016) and more recently in Lamei and Hayatdavoodi (2020).

The incoming wind flow and the wake downstream of the rotor, along with the motion of the platform, result in an unsteady, complicated flow surrounding the blades and the tower. The fully-coupled aeroelastic numerical approaches can obtain the transient structural responses of the blades and the tower to the unsteady aerodynamic loading, see Liu and Xiao (2019) and Rodriguez and Jaworski (2020) among others. In the decoupled approaches, a subset of prescribed mode shapes represents the flexibility of the tower and the blades of a FOWT. Commonly, the mode-shapes of the tower and the blades are obtained with multi-body analysis or finite element method, see e.g. Kim and Kwon (2019), Chen et al. (2019) and Lemmer et al. (2020). However, most of the fully-coupled and decoupled approaches have been limited to flexible blades and towers, whereas the platforms are considered as rigid.

In addition to the coupling of wind turbine aeroelasticity with aerodynamic and hydrodynamic loads, the natural frequencies of the floating structure might be within or near the wave energy spectrum, resulting in potential resonance behaviour of the floating body. Therefore, the coupling between elasticity of the structure (the wind turbine and the platform) and the environmental loads is essential to accu-

ately estimate the responses of a FOWT. This is of more importance for emerging concepts of FOWTs where multiple towers are located on one floating platform, see e.g. Ishihara et al. (2007), Jang et al. (2015), Kang et al. (2017), Lamei et al. (2019, 2022).

Hydroelastic analysis of a FOWT is a relatively new concept which is considered only in a few studies. A common approach is to compute the hydrodynamic loads on the structure with the potential flow theory. The mode-shapes of the floating platform are obtained with finite element analysis or analytical solutions and added as generalized modes to the rigid body degrees of freedom of the structure. The responses of the structure including the effect of the platform flexibility and the sectional forces are obtained in either time- or frequency-domains. In studies by Borg et al. (2017) and Mantadakis et al. (2019), hydroelasticity of the hull of a SPAR-type FOWT is investigated in the absence of aerodynamic loads on the rotor. Hegseth et al. (2018) computed the column bending moment of a braceless semisubmersible hull of an FOWT and compared the results with experimental measurements under wave-only conditions (i.e. in the absence of wind). The coupling effect between the operating rotor and the hydroelasticity of the FOWT is not considered. Li (2022) studied the hydroelastic effect of a barged-shape platform on the power output of the FOWT, and observed that although the flexibility of the platform reduces the tower base bending moment, the instantaneous power output of the wind turbine undergoes high fluctuations up to 22.5%.

In emerging concepts of FOWTs, namely multi-unit FOWTs, multiple wind turbines are supported by a large floating substructure, see Ishihara et al. (2007), Hu et al. (2014), Bae and Kim (2014, 2015), Hanssen et al. (2015), Jang et al. (2015), Kang et al. (2017), Lamei et al. (2019), Bashetty and Ozelik (2020a, b, c). Interest in multi-unit FOWTs is because they may offer reduced cost of installation, marine operations and mooring systems as compared with single-unit FOWTs. However, the hydroelastic behaviour of multi-unit FOWTs might be significant, due to the large characteristic length of their floating substructures. Furthermore, installing multiple wind turbines on a large floating platform influences the elastic deformation of the substructure. Hence, it is essential to investigate the elastic deformation of a multi-unit FOWT and its effect on its loads and motion. Kang et al. (2017) studied the hydroelasticity of a multi-unit FOWT platform in response to wave, wind and current loads in the time-domain. In that study, the wind turbines and the floating platform are assumed as individual bodies and their mode-shapes are computed separately, i.e. the coupling between the elastic motions of the superstructure and the substructure is not considered. Hence, the deformation of the blades and the tower, and the platform have no effect on the hydrodynamic and aerodynamic loads on the structure, respectively.

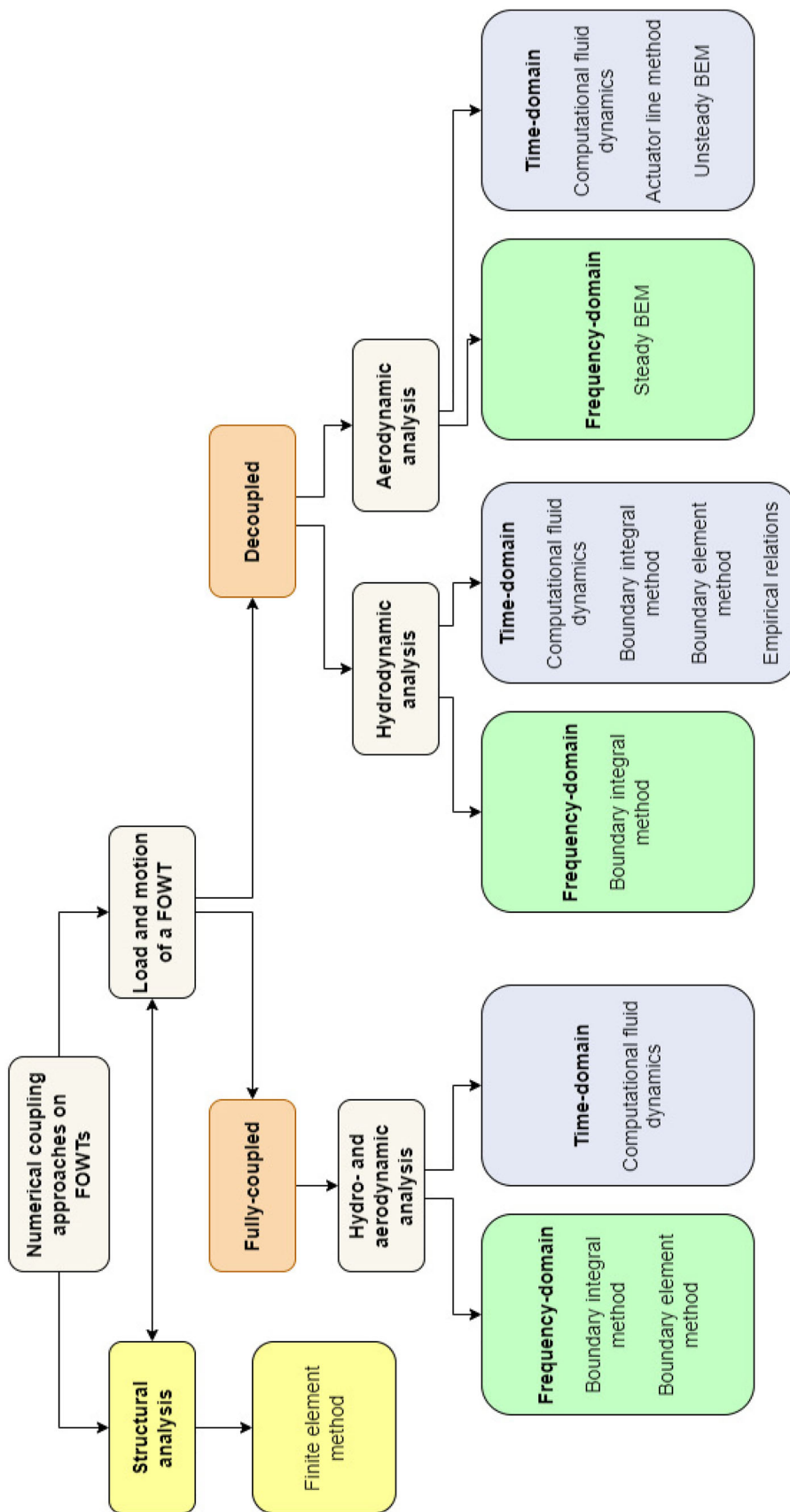


Fig. 1 Numerical approaches applied for structural analysis, hydrodynamic and aerodynamic loads and responses

To the authors' knowledge, elastic deformation of the entire floating substructure of a FOWT (in addition to the superstructure) to combined wind and wave loads has not been considered in any of the existing numerical coupling approaches of FOWTs. For instance, hydroelasticity analysis in OpenFAST, a numerical coupling tool for FOWTs, is only limited to slender or low-stiffness members of the substructure, and the flexibility of large-volume members of the substructure are neglected; see Jonkman et al. (2019, 2020) for more details. In the model developed in this study, we aim to study these questions, namely (i) how the elasticity of the substructure affects the motions of a FOWT to wave loads, and (ii) how the hydroelastic motions of a FOWT changes when the aerodynamic load is added. Furthermore, most previous studies of wind and wave loads on FOWTs are in time domain, and despite an emerging interest on multi-unit FOWTs, the numerical approaches are commonly limited to single-unit FOWTs. In this study, we investigate the elastic motion of FOWTs with a coupling approach in the frequency domain that is not limited to single-unit FOWTs.

Aeroelastic response of a FOWT is typically computed with prescribed mode-shapes of the blades and the tower. However, the mode-shapes are computed for a single blade and the tower in the absence of the rotor and the substructure, i.e. the coupling between the rotor, the tower and the substructure on elastic deformation of the blades and the tower is not considered. If the structural response of the substructure is of interest, its deformation to wave loads only (in the absence of the aerodynamic loads on the rotor and the towers) are investigated and hence, the effect of aeroelasticity and hydroelasticity on each other (i.e. the aeroelastic and hydroelastic coupling) is not considered.

We are considering an approach here to investigate the aeroelastic responses of FOWTs in a more complete manner. A hydro-aero-elastic coupling approach is essential to account for the elasticity of the entire FOWT. This is especially true for concepts with large substructures or multi-unit FOWTs, although the elastic motion of a single-unit FOWT, depending on its platform characteristics and the material properties of the complete structure, can be significant. Furthermore, structural analysis should be carried out for the complete structure to account for structural coupling between the wind turbines and the floating platform. Larger wind turbines with higher capacities are used in deep waters, which come with larger towers, rotors and substructures. Therefore, the effect of both aero- and hydrodynamic loads on the elasticity of the structure should be investigated. For this purpose, an approach that is applicable to both single- and multi-unit FOWTs is desirable as it provides important information regarding the rigid body and elastic deformation of the structure within reasonable computational resources.

This paper aims to introduce an approach to determine the hydroelastic and aeroelastic responses of single- and

multi-unit FOWTs to combined wind and wave loads in frequency-domain, see Lamei et al. (2022) for hydro- & aeroelastic analysis of a multi-unit FOWT. The numerical tool includes integrated modules for hydrodynamic, aerodynamic and elastic analysis of the complete structure of a FOWT. In Sects. 2 and 3, the background theory on motion and load analysis of rigid and fully flexible FOWTs to combined wind and wave loads is explained. This is followed in Sect. 4 by the introduction of the numerical approach for hydroelasticity and aeroelasticity analyses of FOWTs. Our goal in this paper is to introduce an approach to determine motion and elastic responses of a FOWT of arbitrary shape and with arbitrary number of towers. After the presentation of the complete model, in Sects. 5 and 6, we apply this approach to investigate responses of a SPAR FOWT, for which there are available experimental data allowing us to compare. Finally, concluding remarks regarding the performance of the numerical approach is provided.

2 Rigid body analysis

Wave, current and wind loads, and restoring forces and moments are the dominant external loads that influence the motion of a FOWT. Here, we focus on rigid body analysis of a FOWT to wave and wind loads and the mooring forces, see Fig. 2. In our linear analysis approach in the frequency domain, the wind load is modelled with a harmonic function with the incoming wave frequency, ω . In this approach, the wind effect consists of two major components, namely (i) the wind-induced load on the structure, and (ii) the damping effect due to the relative motion of the floating body and the incoming wind (discussed in the following section, Sect. 2.2).

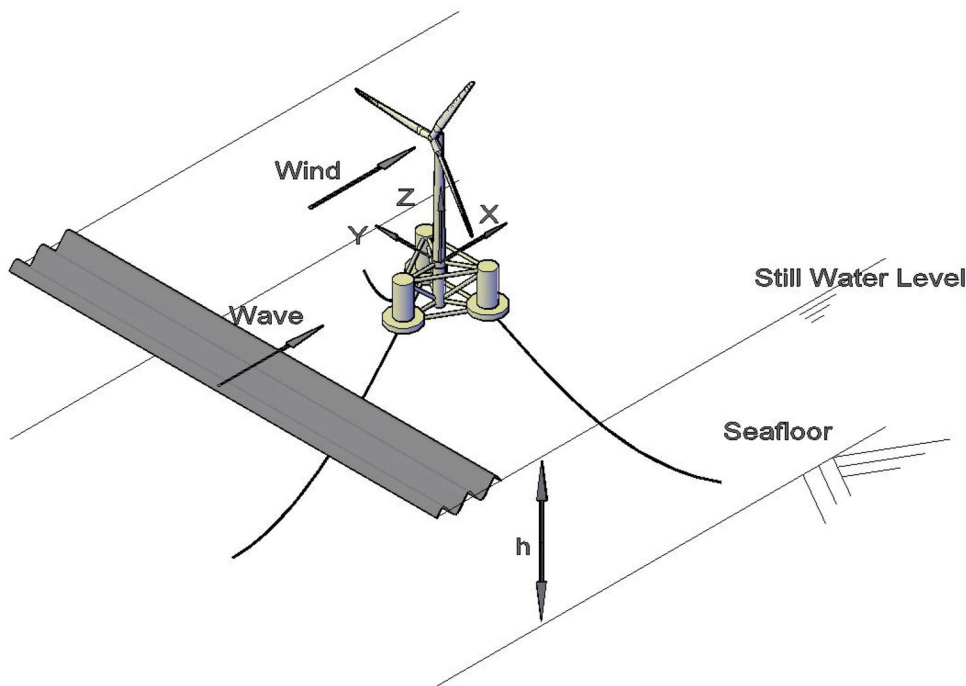
Newton's second law for a FOWT under the action of combined wave and wind loads, the mooring forces F_{moor} and hydrostatic restoring loads F_{hst} takes the form of

$$F_{\text{wave}} + F_{\text{wind}} + F_{\text{moor}} + F_{\text{hst}} = -\omega^2 M \xi, \quad (1)$$

in the frequency domain, where M is the mass matrix of the floating structure and ξ is the complex body response phasor. Equation (1) represents a system of equations and the responses of the structure and the environmental loads are given as vectors for translational and rotational rigid body modes.

Linear diffraction wave theory combined with blade element momentum method are used to obtain the hydrodynamic and aerodynamic loads on a FOWT. The methods and their formulations are presented in the following subsections.

Fig. 2 Schematic diagram of the interaction of waves and wind with a FOWT. In the approach developed in this study, the type and geometry of the structure, and mooring lines, wave direction and water depth, h , are arbitrary



2.1 Hydrodynamic loads

The interaction of waves with the floating platform is described by linear diffraction wave theory, where the fluid is inviscid and incompressible and the flow is irrotational. Waves are assumed small-amplitude and the wave-induced motions and rotations of the structure are linearly proportional to the wave amplitude. Here, the hydrodynamic loads and consequently motions of the floating structure due to the terms of the second and higher order of the wave amplitude are not considered.

An earth-fixed Cartesian coordinate system is defined on the still water level, shown in Fig. 2, where its x -axis is parallel with the incoming headsea waves, and its z -axis points upwards. The rigid body translational motion of the floating body along x -, y - and z -axes are surge (ξ_1), sway (ξ_2) and heave (ξ_3), respectively and its rotational motion about x -, y - and z -axes are roll (ξ_4), pitch (ξ_5) and yaw (ξ_6), respectively.

In linear diffraction theory, both the motion of the structure and the hydrodynamic loads are harmonic with the wave frequency. The total hydrodynamic force on the structure, F_{tot} , is the sum of the wave excitation loads (sum of Froude-Krylov and diffraction forces), $F_{exciting}$, loads due to the added mass and hydrodynamic damping components, F_{hydro} , hydrostatic restoring terms, F_{hst} , and mooring forces, F_{moor} . In the linear equation of motion, the forces of the mooring lines can be modelled with a stiffness matrix. Hence, Eq. (1), in the absence of the wind loads, takes the form:

$$F_{j,tot} = F_{j,exciting} + F_{j,hydro} + F_{j,hst} + F_{j,moor}$$

$$= -\omega^2 M_{jk} \xi_k, \quad j, k = 1, 2, \dots, 6, \tag{2}$$

where M_{jk} is the body mass matrix, and ξ_k is the complex body response phasor in mode k . Consistent with the linear wave theory, the equation of motion can be written as (Wehausen and Laitone 1960):

$$\xi_k (-\omega^2 (M_{jk} + a_{jk}) + i \omega b_{jk} + c_{jk,hst} + c_{jk,moor}) = A X_j, \quad j, k = 1, 2, \dots, 6, \tag{3}$$

where a_{jk} and b_{jk} are the frequency-dependent added mass and hydrodynamic damping coefficients, $c_{jk,hst}$ and $c_{jk,moor}$ represent the hydrostatic restoring coefficient, and the mooring stiffness, A is the wave amplitude, and X_j is the complex amplitude of exciting force or moment for a unit wave amplitude in mode j , hence $F_{j,exciting} = A X_j$.

2.2 Aerodynamic loads

In this section, discussion is provided on how the aerodynamic load is determined, and how it is added to the equation of motion of a FOWT under combined steady wind and wave loads in the frequency domain. In this study, the magnitude of the thrust force is computed by steady BEM and the phase angle of the aerodynamic force and its induced moment on a FOWT is determined analytically.

2.2.1 Steady BEM

Steady BEM is applied to estimate the magnitude of aerodynamic loads on the rotor. BEM is based on the conservation of mass and the axial and angular momentum balances. Air is assumed to be incompressible and inviscid and the incoming airflow is axisymmetric with respect to the rotor. In our BEM model, the effect of dynamic wake and stall, and yaw misalignments and gyroscopic effects are not considered, see e.g. Hansen et al. (2006) and Hansen (2007). The gyroscopic effect on the motions of a FOWT, particularly on its pitch and yaw motions, are discussed in Chen et al. (2021) and Høeg and Zhang (2021). The present study only focuses on quasi-steady aerodynamic forces on the rotor and the effect of the presence of the hub and the tower on the aerodynamic load on the rotor are not considered (though the wind load on the tower is calculated).

In BEM, the rotor is presented as a disk with an infinite number of blades. Control volumes are defined along the blades and the normal and tangential forces are computed. Integration of the aerodynamic normal forces over the blades equals to the thrust force acting at the hub centre of the rotor. The total thrust force over the rotor plane area is obtained by,

$$T = \frac{1}{2} C_T \rho V_0^2 A_r, \quad (4)$$

where V_0 is the incoming wind speed, ρ is the air density, and A_r and C_T are the rotor plane area and the thrust coefficient of the rotor, respectively.

2.2.2 Aerodynamic load on a fixed offshore wind turbine

The aerodynamic thrust force on a fixed wind turbine is given with a harmonic function with wave frequency so that it can be linearly added to the governing equation of motion of the floating structure, Eq. (3). In this approach, the aerodynamic load on the wind turbine is treated similarly to the wave loads on the substructure of the wind turbine. Furthermore, it is assumed that $F_{j,W}$ is an excitation force in surge acting at the top of the structure by the incoming wind. The wind excitation force has the same frequency as the incident waves, ω , and the wind direction is always orthogonal to the rotor, parallel to the x -direction. This assumption is made to allow adding directly the wind effect to the hydrodynamics equations of motion of the body and solve the system of equations in the frequency domain. To consider the misalignment between the incoming waves and the wind on the rotors, the wave heading angle is changed. That is, the wind always acts in the $+x$ -direction, see Fig. 2, but the wave can act in any direction (Lamei et al. 2022). We note that in this approach, no restriction is made about the magnitude of the wind speed (and consequently, the magnitude of the wind load). Further

discussion on the linear presentation of the aerodynamic load on FOWTs can be found in Kvittem and Moan (2014), Lupton (2014), Wang et al. (2016), Pegalajar-Jurado et al. (2018) and Karimi et al. (2019), who have applied this assumption to analyse response of FOWTs to wave and wind loads.

We assume that the integrated aerodynamic normal force over the blades act at the hub centre and eventually is transferred to the tower top. Given that the wind turbine towers are commonly circular cylinders, and the wind load is assumed harmonic with frequency ω , we determine the wind load phase angle following the approach proposed by MacCamy and Fuchs (1954) for wave-interaction with a circular cylinder i.e.

$$F_{j,W} = |F_{j,W}| \cos(\omega t - \delta_{\text{aero}}), \quad j = 1, 2, \dots, 6, \quad (5)$$

where δ_{aero} is the phase angle of the inline force and it is determined as

$$\delta_{\text{aero}}(kr_0) = -\tan^{-1} \left[\frac{Y'_1(kr_0)}{J'_1(kr_0)} \right], \quad (6)$$

in which $J_p(kr)$ and $Y_p(kr)$ are the Bessel functions of the first and the second kind of order p , respectively, and r_0 is the diameter of the top of the tower. Therefore, the harmonic aerodynamic load on a fixed rotor in surge, Eq. (5), can be represented with its magnitude computed by Eq. (4), i.e.

$$F_{1,W} = \frac{1}{2} C_T \rho V_0^2 A_r \cos(\omega t - \delta_{\text{aero}}), \quad (7)$$

2.2.3 Aerodynamic load on a FOWT

The governing equations of a floating structure, Eq. (3), are solved for frequency ω . To account for the aerodynamic load on the structure in the frequency domain, similar to the aforementioned fixed wind turbine, the aerodynamic load is linearized with a harmonic function of frequency ω . The thrust force on a FOWT is computed for the incoming wind velocity relative to the rotor. Assuming that the speed at the tower top along the direction of the incoming wind, \dot{x} , is small the thrust force with the relative incoming wind speed can be approximated by the Taylor series. For the thrust force with incoming wind speed V_0 and deviations of $V_{\text{rel}} = V_0 - \dot{x}$ about V_0 , we can write

$$T(V_{\text{rel}}) = T(V_0) - \dot{x} \frac{\partial T(V_0)}{\partial V_0} + O(\dot{x}^2) + \dots \quad (8)$$

where the terms containing \dot{x}^2 and higher orders in Eq. (8) are discarded in this linear approach. In the frequency domain, assuming the motion of the structure due to the horizontal wind is restricted in xz -plane, the horizontal speed at the hub of the rigid structure, \dot{x} , is given as $i\omega(\xi_1 + \xi_5(z_h - z_{cg}))$,

where z_h and z_{cg} are the vertical coordinates of the hub centre and the centre of gravity of the FOWT. Thus, Eq. (8) can be rewritten as

$$T(V_{rel}) = \underbrace{T(V_0)}_{F_{1,W}} - i\omega(\xi_1 + \xi_5(z_h - z_{cg})) \frac{\partial T(V_0)}{\partial V_0}, \quad (9)$$

and $V_{rel} = V_0 - i\omega(\xi_1 + \xi_5(z_h - z_{cg}))$ is the relative incoming wind velocity to the rotor. Moreover, the first term at the right-hand side of Eq. (9) is equal to the thrust force on a rotor of a fixed wind turbine, $F_{1,W}$. The second term is a function of both incoming wind speed and the speed of the structure at the hub centre. Hence, substituting Eq. (8) into Eq. (9) reads

$$\begin{aligned} T(V_{rel}) &= F_{1,W} - i\omega(\xi_1 + \xi_5(z_h - z_{cg})) \times [\rho C_T A_r V_0], \\ T(V_{rel}) &= F_{1,W} - i\omega(\xi_1 + \xi_5(z_h - z_{cg})) \times B_{aero}. \end{aligned} \quad (10)$$

where $B_{aero} = \rho C_T A_r V_0$ represents the aerodynamic damping coefficient.

The wind load vector F_W , at the centre of gravity of a FOWT with six degrees of freedom, consists of a force component in surge which is the thrust force, and the induced moment by the thrust force at the centre of gravity in pitch. If the hub of a single-unit FOWT is along a vertical line passing through the centre of gravity of the structure, the aerodynamic load vector F_W can be defined with the computed $|F_{j,W}|$ component in Eq. (5) and the phase angle δ_{aero} in Eq. (6). Therefore, F_W is

$$F_W = \begin{bmatrix} |F_{1,W}| \\ 0 \\ 0 \\ 0 \\ -|F_{1,W}| \times (z_h - z_{cg}) \\ 0 \end{bmatrix} \cos(\omega t - \delta_{aero}) \quad (11)$$

For a single wind turbine located above the centre of gravity of the floating body, it is assumed that its thrust force and aerodynamic damping effect is significantly larger in surge than in sway direction. Since the damping effect in sway is negligible, only the terms in surge, pitch and their coupling components in $B_{aero\,mat}$ are nonzero:

$$B_{aero\,mat} = \begin{bmatrix} \rho C_T A_r V_0 & 0 & 0 & 0 & \rho C_T A_r V_0(z_h - z_{cg}) & 0 \\ 0 & 0 & 0 & 0 & 0 & 0 \\ 0 & 0 & 0 & 0 & 0 & 0 \\ 0 & 0 & 0 & 0 & 0 & 0 \\ \rho C_T A_r V_0(z_h - z_{cg}) & 0 & 0 & 0 & \rho C_T A_r V_0(z_h - z_{cg})^2 & 0 \\ 0 & 0 & 0 & 0 & 0 & 0 \end{bmatrix}, \quad (12)$$

where $B_{aero\,mat}$ in rotational modes contains the effect of the offsets of the hub centre from the centre of gravity.

To obtain the motions of the structure to combined wind and wave loads, the aerodynamic load vector, Eq. (11), and its damping effect, Eq. (12), are added to Eq. (3) as

$$\begin{aligned} \xi_k (-\omega^2(M_{jk} + a_{jk}) + i\omega b_{jk} + c_{jk,hst} + c_{jk,moor}) \\ = A X_j + \underbrace{(F_{j,W} - i\omega \xi_k B_{jk,aero})}_{\text{aerodynamic effect by the operating rotor}}, \quad (13) \\ j, k = 1, 2, \dots, 6. \end{aligned}$$

Rearranging Eq. (13) by moving the aerodynamic damping coefficients to the left-hand side would read

$$\begin{aligned} \frac{\xi_k}{A} (-\omega^2(M_{jk} + a_{jk}) + i\omega(b_{jk} + B_{jk,aero}) + c_{jk,hst} \\ + c_{jk,moor}) = X_j + \frac{F_{j,W}}{A}, \\ j, k = 1, 2, \dots, 6. \end{aligned} \quad (14)$$

The RAOs of a rigid FOWT to combined wind and wave loads, $|\frac{\xi_k}{A}|$, are obtained by solving Eq. (14) for a range of frequencies, ω .

3 Flexible body analysis

The elastic responses of a FOWT are obtained using a reduced basis approach. In this method, the structural deformations are represented by a linear superposition of mathematical mode-shapes that are sufficiently general to model the physical motion of the structure, see for instance Bishop et al. (1986), Newman (1994) and Wu et al. (1993) for more details. Therefore, in the linearized frequency-domain analysis, in addition to the rigid-body modes, the mode-shapes are added as generalized modes to form the total degrees of freedom (rigid and flexible modes combined) of the flexible structure.

The mode-shapes of the full structure are determined with the finite element method. The mode-shapes of a floating structure can be represented by a subset of free undamped wet deformation modes of the structure in water or dry modes of the structure in air. However, the wet natural frequencies of a floating structure depend on the added mass at a given wave frequency. Hence, an iterative process is required to obtain the wet eigenfrequency. In this study, the dry mode shapes of the full structure including the rotor and the tower of a FOWT are considered together, and hence the problem is defined with a subset of m dry modes from the total possible

modes, N , of the flexible structure. The coupling between the structural deformation of the blades and their rotational motion would modify the structural stiffness, and hence its mode shapes, see for instance Chen et al. (2023) for more details. We note that the effect of the rotation of the blades on mode shapes is not included in our analysis.

When a floating structure is displaced from its equilibrium position, the hydrostatic restoring coefficients depend on both the change of hydrostatic pressure as external forces and the internal stresses. An explicit formulation of hydrostatic restoring coefficient is obtained by linearizing both the internal and external generalized forces on the floating body, see Huang and Riggs (2000). The complete formulation accounting for contributions of both internal stresses, c^g , and hydrostatic pressure, c^f , is given by

$$c_{\text{hst}} = c^f + c^g. \quad (15)$$

The complete hydrostatic restoring coefficient, $c_{ij,\text{hst}}$ is computed as

$$\begin{aligned} c_{ij,\text{hst}} = & -\rho_w g \int_{S_b} \psi_k^i (\psi_3^j + z \epsilon_v^j) n_k \, dS \\ & + \rho_w g \int_{S_b} z \psi_l^i \psi_{k,l}^j n_k \, dS + \int_{\Omega_s} \sigma_{ln} \psi_{k,l}^i \psi_{k,n}^j n_k \, d\Omega, \\ & k, l, n = 1, 2, 3, \quad i, j = 1, 2, \dots, m, \end{aligned} \quad (16)$$

where ρ_w is the mass density of water, g is the gravitational acceleration, and S_b is the wetted surface. ψ_k^i is the displacement in mode i , i representing both rigid-body modes and the elastic generalized modes. n_k is the k th component of the normal vector on the wet surface. Ω_s is the structural volume, σ_{ln} is the structural stress under gravitational loads in calm seas, ϵ_v^j is the volumetric strain in mode j . In Eq. (16), the first two integrals represent the hydrostatic pressure and the last one represents the internal stresses.

For a flexible FOWT under the action of combined wind and wave loads, the frequency-domain equation of motion, Eq. (14), with the addition of the generalized modes, takes the form of

$$\begin{aligned} \frac{\xi_k}{A} (-\omega^2 (M_{jk} + a_{jk}) + i\omega (b_{jk} + B_{jk,\text{aero}}) + c_{jk,\text{hst}} \\ + c_{jk,\text{moor}}) = X_j + \frac{F_{j,W}}{A}, \\ j, k = 1, 2, \dots, m. \end{aligned} \quad (17)$$

where the hydrostatic coefficient, $c_{jk,\text{hst}}$ is computed by Eq. (16) and m is the total number of modes of the FOWT. The first six translational and rotational modes are normalized by unit-displacements and the added generalized modes are normalized by mass of the structure.

4 Numerical solution

A three-dimensional finite element model of the blades, the tower and the platform of a FOWT is generated with shell elements, and the rotor-nacelle-assembly (RNA) is modelled with mass points at the top of the tower. The catenary cables are modelled with an element based on small strain elastic catenary theory and the taut cables are modelled as springs. The generalized mass and stiffness matrices are computed by assigning the material properties of the shell elements over the entire structure.

Assuming that the displacements of the structure are harmonic and described with a subset of m modes, an eigenvalue analysis results in:

$$(C_s - \omega_{n,j}^2 M_s) \Psi_{n,j} = 0, \quad j = 1, \dots, m, \quad (18)$$

in which $\omega_{n,j}$ and $\Psi_{n,j}$ are the natural frequency and the mode shape in mode j of the structure, and M_s and C_s are the structural mass and stiffness matrices, respectively. The displacement of the body is presented with a linear combination of the mode shapes for m modes, where the first six mode shapes represent the rigid body modes of the structure and $j > 6$ refer to the generalized modes due to the flexibility of the structure.

The rigid body responses of a FOWT with the aerodynamic load as an integrated force at the hub centre, and as distributed normal forces over the rotor were computed and compared. Similar aerodynamic thrust forces were obtained by both approaches, however, for a detailed structural analysis of the rotor under aerodynamic load, the normal force components and the local damping coefficients are distributed over the front face of the rotor. With finite element analysis, the magnitude of the total aerodynamic load vector and the global aerodynamic damping matrix at the centre of gravity of the floating structure is computed. This approach is particularly different from the existing numerical coupling tools on FOWTs where the thrust force is pre-calculated and added directly to the hub centre.

To calculate the distributed aerodynamic force components on the rotor, first the nodes of the blades facing the incoming wind are identified. With BEM, the aerodynamic normal forces and their corresponding local aerodynamic damping coefficients on each control volume across the blades are computed and distributed over the blades as nodal forces and dampers.

The amplitude of the aerodynamic load on the tower is computed by

$$F_D = \frac{1}{2} C_d A_t V_0^2, \quad (19)$$

where $C_d = C_d(\text{Re})$ is the drag coefficient with respect to the incoming wind Reynolds number (see Hoerner 1958), $\text{Re} = \frac{V_0 D}{\nu}$, where D is the diameter of the tower, and ν is the kinematic viscosity of air at 20°, and A_t is the cross-sectional area of the tower. Similar to the blades, the wind load on the tower computed by Eq. (19) is distributed over the front face nodes of the tower. The equivalent aerodynamic load vector and damping effect matrix on the centre of gravity of the FOWT are obtained with the aerodynamic thrust force and damping coefficient distributed over the rotor and the aerodynamic drag force on the tower.

In the hydrodynamic analysis, the finite element model of the structure is mapped to a panel mesh covering the wetted surface of the platform. The diffraction and radiation problem over the wet panels are solved by the boundary integral equations, with three dimensional source distribution, Green function method, see Wehausen and Laitone (1960), Wang et al. (1991) and Ertekin et al. (1993) among others. Here, with the boundary integral equations, the square matrices of the frequency-dependent hydrodynamic coefficients and wave exciting force vectors for rigid body modes and added generalized modes are computed. The structural and hydrodynamic viscous damping effects, if considered, are added to the damping terms at the left side of the equation of motions, Eq. (17). Finally, the mass and stiffness matrices are obtained by FEM and the governing equation of motion, Eq. (17), is solved with standard matrix solvers in the frequency domain, for m modes including the flexibility of the full structure, and the combined wind and waves loads.

The computations explained above are performed in HYDRAN-XR (see NumSoft Technologies 2020), a potential-flow solver for hydrodynamic analysis, integrated with finite element analysis for structural considerations. HYDRAN-XR has been enhanced to include the blade element momentum method solver for the aerodynamic analysis of the wind turbines. Figure 3 presents a flowchart of the three aforementioned integrated numerical solvers developed for structural, aerodynamic, and hydrodynamic analysis of a FOWT.

5 Results: rigid body responses

In this and the following sections, we will apply the model discussed in the previous sections to investigate responses of a FOWT, for which there are available data for comparisons. Our goal is to assess and demonstrate the performance of the model. The hydro-aero-elastic computational model discussed in the previous sections is applied to determine the hydrodynamic and aerodynamic loads on a SPAR FOWT and study its rigid body responses. Results are compared with the laboratory experiments and other numerical solutions where possible. The simulations are carried out on a

desktop machine with Intel Core *i5* 6500U, 3:20 GHz CPU and 32 GB memory.

A SPAR FOWT is considered in the Offshore Code Comparison Collaboration (OC3) project (see Jonkman 2010; Jonkman and Musial 2010). In this concept, a 5 MW national renewable energy laboratory (NREL) wind turbine (Jonkman et al. 2009) is supported by a SPAR platform. In an experimental study by Ahn and Shin (2017), the responses of a rigid model of the SPAR FOWT (with a scaling ratio of 1:128) to regular and irregular waves, and combined wave and wind conditions are measured and compared with their corresponding numerical results by FAST coupled with an in-house potential flow solver at the University of Ulsan, namely UOU. The wind loads on the model corresponds to zero and rated wind speed, 11.4 m/s for the 5 MW wind turbine. For the latter wind load, following the Froude scaling law, the rotor model is operated with a speed 136.9 revolutions per minute at a wind speed of 1.007 m/s.

The SPAR platform is made of steel and it is moored to the seabed with three slack catenary mooring lines. The draft of the structure is 120 m and the water depth at the installation site is 320 m. The platform is made of two connected cylinders, one with 9.4 m diameter at the bottom tapered to a more slender cylinder with 6.5 m diameter at the top. Information about the mass distribution, mooring configuration and characteristics, the installation site of the SPAR FOWT and the added linear viscous damping coefficients are obtained from Jonkman (2010) and Ahn and Shin (2017), respectively and presented in Table 1.

The SPAR FOWT is modelled using the prototype dimensions. The mesh convergence study is carried out for panel sizes 0.5, 1 and 1.5 and the RAOs for the different meshes were compared in translational and rotational modes. The responses of the FOWT were converged with panel size 1 m. With the converged panel size and 3966 wet panels, the aeroelastic and hydroelastic analysis of SPAR FOWT by HYDRAN-XR requires approximately 3 h for 122 wave-wind frequencies. For comparison, in FAST, analysis of the aerodynamic loads on the rotor of the SPAR FOWT, takes about 30 min for a single wave frequency (see Jonkman et al. 2018). Hence, running FAST for 122 wave frequencies, as considered here, would require about 61 h. Moreover, the time that is required for the hydrodynamic analysis (by a potential flow solver) should also be added to the computational cost of FAST.

In Fig. 4, the added mass and damping coefficients in surge, heave and pitch, and the surge and pitch coupling components are compared with numerical results computed by WAMIT (see Jonkman et al. 2009). A very good agreement between the hydrodynamic frequency-dependent coefficients reported by Jonkman et al. (2009) and computed by HYDRAN-XR is observed.

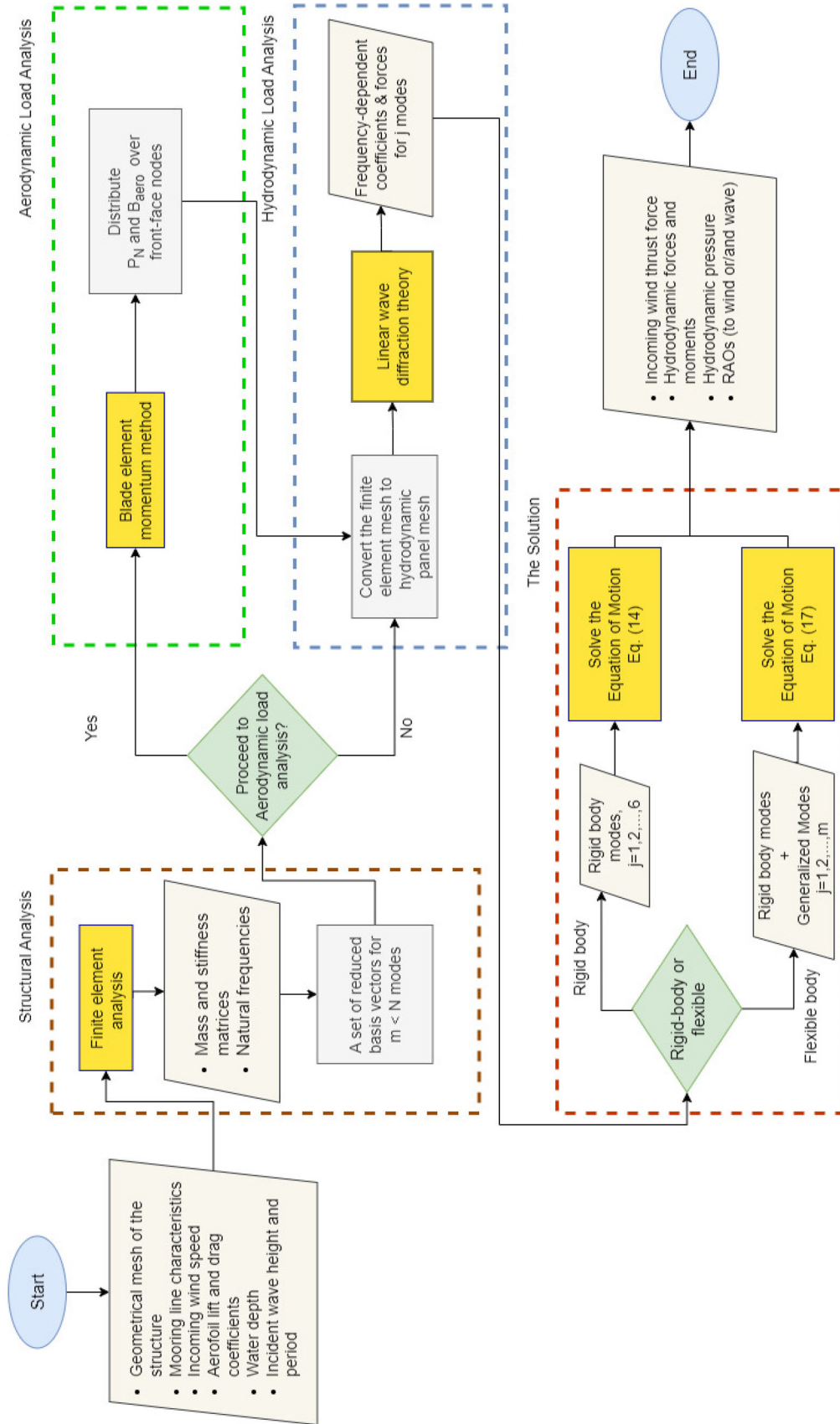


Fig. 3 The flowchart used to investigate the motion and elastic responses of a FOWT in HYDRAN-XR

Table 1 Mass distribution and mooring lines characteristics of the OC3 SPAR FOWT reported by Jonkman (2010) and hydrodynamic viscous damping coefficients given by Ahn and Shin (2017)

Mass distribution	
Total mass (kg)	8.07×10^6
Centre of gravity, C_{CG} below SWL (m)	78.0013
Roll inertia about C_{CG} (kg m^2)	2.10×10^{10}
Pitch inertia about C_{CG} (kg m^2)	2.10×10^{10}
Yaw inertia about C_{CG} (kg m^2)	1.79×10^8
Viscous damping coefficients	
Additional linear damping in surge (N/(m/s))	5×10^4
Additional linear damping in sway (N/(m/s))	10×10^4
Additional linear damping in heave (N/(m/s))	3×10^5
Additional linear damping in yaw (N/(rad/s))	1.3×10^6
Mooring line characteristics	
Number of mooring lines	3
Angle between the mooring lines ($^\circ$)	120
Depth of anchors (m)	320
Depth of fairleads (m)	70
Mooring line diameter (m)	0.09
Equivalent mooring line weight in water (N/m)	698.09
Equivalent mooring extensional stiffness (N)	3.84×10^8
Additional yaw spring stiffness (N m/rad)	9.83×10^7

Figure 5 presents the computed rigid-body wave-induced motions of the SPAR FOWT. The numerical responses by HYDRAN-XR are compared with the laboratory experiments and the numerical results of Ahn and Shin (2017) in surge, heave and pitch. Ahn and Shin (2017) obtained the motion of the SPAR FOWT to wave loads by using FAST + UOU. The wet natural frequencies of the SPAR FOWT in heave and pitch are approximately 31 s and at wave frequency $\omega = 0.2 \text{ rad/s}$. Consequently, heave and pitch RAOs experience a peak at $\omega = 0.2 \text{ rad/s}$, and similarly surge responses show a local maximum at the same frequency due to the coupling effect between the surge and pitch motions. The same behaviour at $\omega = 0.2 \text{ rad/s}$ is observed in surge, heave and pitch in experimental and numerical results of Ahn and Shin (2017). As explained by Ahn and Shin (2017), the experimental data are slightly underestimated due to the extra resistance from the bundle of the signal cables, the effect of which is observed in particularly surge and pitch RAOs. Nevertheless, the numerical results are in a very good agreement with the laboratory measurements.

Next, the aerodynamic load analysis in HYDRAN-XR is compared with two experimental benchmarks. First, for the 5 MW rotor, the aerodynamic thrust force is computed and compared with experimental data on the model scale. Afterwards, the motions of the SPAR FOWT to combined wind and wave loads are computed and compared with available laboratory measurements.

The wind thrust force on the rotor is the main aerodynamic load contribution on the global motion of a FOWT.

To assess the performance of the aerodynamic analysis of HYDRAN-XR, wind load on a fixed 5 MW NREL rotor is computed and compared with experimental measurements. Coulling et al. (2013) carried out laboratory experiments of combined wave and wind interactions with a 1:50 model scale of 5 MW NREL FOWT and compared the measured thrust on the scaled rotor with numerical results computed by unsteady BEM solver of FAST. In these experiments, the incoming wind speed is increased to obtain the Froude-scaled thrust force on the model. For the applied wind speeds, the tabulated lift and drag coefficients of the 5 MW NREL wind turbine (Jonkman et al. 2009) are not provided. Hence, Coulling et al. (2013) calculated the new lift and drag coefficients corresponding to the wind speeds in the experiments and modified the numerical model in FAST.

The total thrust force for the scaled rotor is computed in HYDRAN-XR with respect to the modified airfoil coefficients. The numerically computed thrust forces by HYDRAN-XR and FAST are compared with laboratory measurements of Coulling et al. (2013) in Fig. 6. Shown in Fig. 6, the wind thrust forces on the hub obtained by HYDRAN-XR are in close agreement with the laboratory measurements of Coulling et al. (2013). Moreover, the thrust forces determined by steady BEM in HYDRAN-XR are slightly over-estimated when compared to the unsteady BEM results of FAST, with maximum 7% difference.

Next, the total hydrodynamic and aerodynamic loads on the OC3 SPAR FOWT and their RAOs to combined wind and wave loads are computed in HYDRAN-XR and discussed.

Fig. 4 Comparison of added mass and damping coefficients computed by HYDRAN-XR and the results by WAMIT reported by Jonkman (2010)

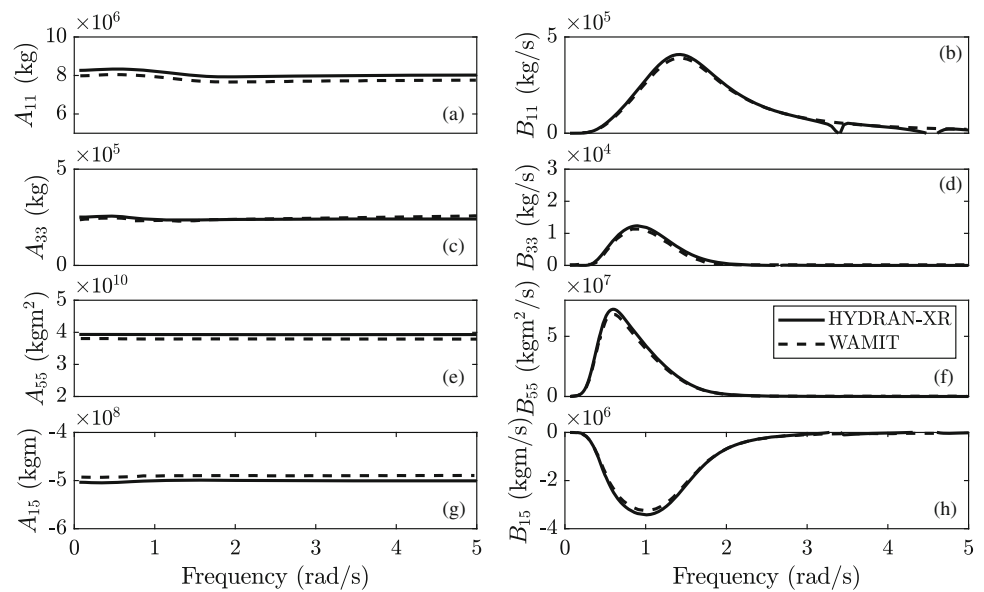
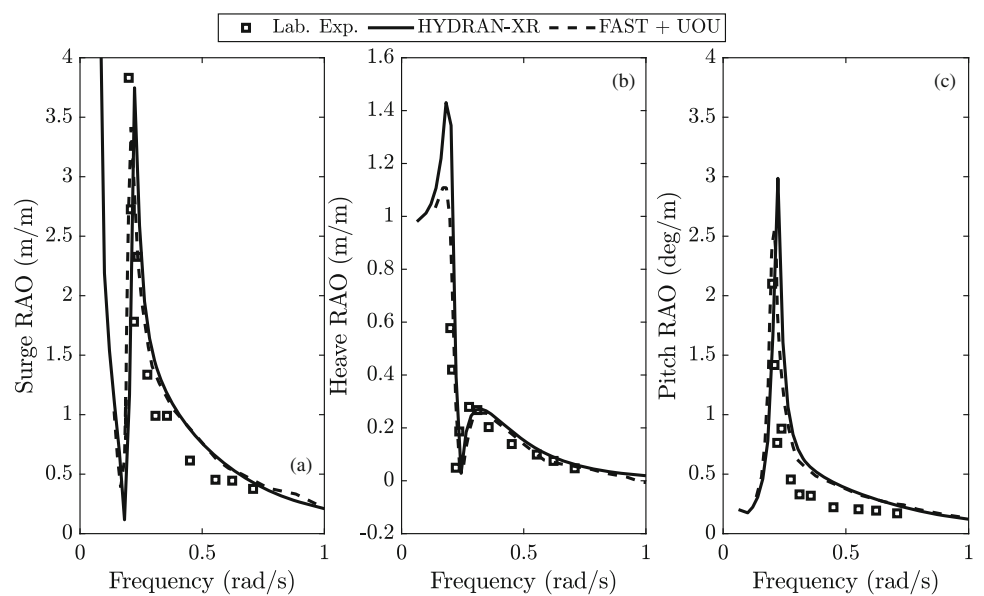


Fig. 5 Comparison of the wave-induced RAOs of the SPAR FOWT computed by HDYRAN-XR and the laboratory measurements of Ahn and Shin (2017)



The simulation is carried out for regular waves with $A = 3$ m (chosen arbitrarily for a representative comparison) and steady wind at 11.4 m/s (rated wind speed). In this study, both wind and wave loads are codirectional.

The horizontal hydrodynamic excitation force with 3 m wave amplitude on the FOWT varies from 500 to 3600 kN for $\omega \leq 1$ rad/s, whereas the thrust force on the 5 MW NREL rotor is considerably smaller, and it is constant at approximately 770 kN. Ahn and Shin (2017) determined the responses of the SPAR FOWT to the same environmental conditions numerically by FAST + UOU and measured the surge, heave and pitch motions of the structure. Figure 7 shows the comparison of the numerical results obtained in HYDRAN-XR and those reported by Ahn and Shin (2017).

From the results, we observe that due to the aerodynamic damping by the operating rotor, peaks in surge and pitch motion of the FOWT to combined waves and wind are smaller than those in wave-induced surge and pitch RAOs, see Fig. 7 for comparison. As expected, the aerodynamic load on the FOWT does not contribute to heave, and responses in heave are identical to the heave RAOs presented in Fig. 5b. The numerical results in HYDRAN-XR in surge and pitch are slightly overestimated compared with the laboratory measurements, however, they are in a very good agreement with the numerical results of Ahn and Shin (2017) by FAST + UOU. Similar to Fig. 5, the difference could be due to added resistance by the signal cables during the experiments, see Ahn and Shin (2017) for more details. Overall,

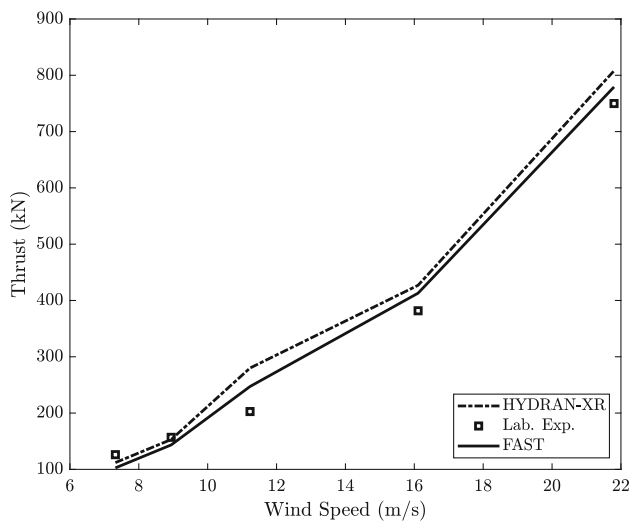


Fig. 6 Comparison of the thrust force on a fixed 5 MW NREL model computed by HYDRAN-XR, and the reported numerical results by FAST and the laboratory measurements of Coulling et al. (2013)

a good agreement is observed between the RAOs obtained by HYDRAN-XR and the laboratory measurements.

6 Results: flexible body responses

Analysis of elastic responses of the entire structure of FOWTs (including the floating body and the turbines), as developed in this study, is particularly critical when the size and the shape of the structure is such that the wave-wind frequency is comparable to the natural frequencies of the structure. This is observed, for example, in the multi-unit FOWTs (Bae and Kim 2014; Hanssen et al. 2015; Lamei et al. 2022), and

Fig. 7 Comparison of the wind- and wave-induced RAOs of the SPAR FOWT computed by HYDRAN-XR and laboratory measurements of Ahn and Shin (2017)

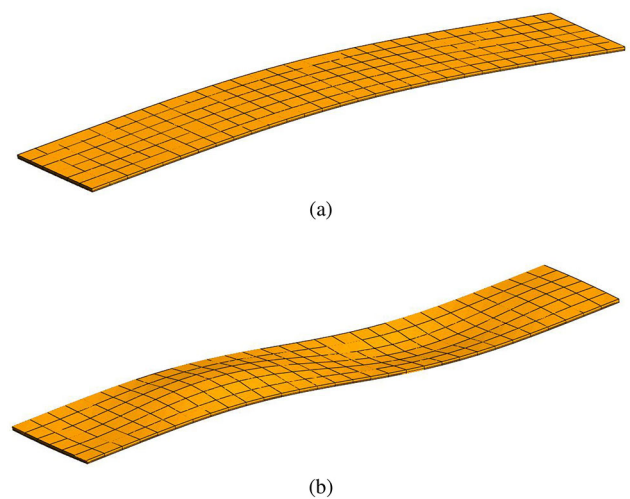
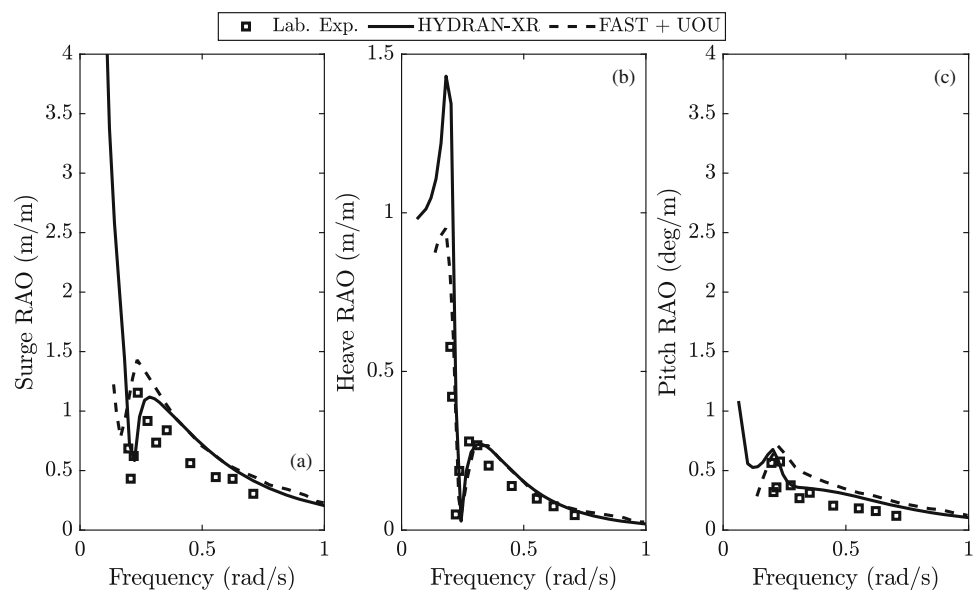


Fig. 8 The **a** 7th and **b** 8th mode-shapes of the flexible barge, at its dry natural periods of $T_n = 0.640$ s and $T_n = 0.294$ s

other floating concepts. To assess the hydroelastic results of HYDRAN-XR, we first consider a barge-shaped platform, for which there are available laboratory data for its hydroelastic responses. Barges are widely used as the floating part of several FOWTs, see e.g. Jonkman (2007) and Chuang et al. (2021). In the following discussion, laboratory measurements of wave interaction with a flexible floating barge are considered and results are compared. Next, we confine attention to the SPAR FOWT considered in the previous section, for the elastic analysis to determine deformation and wave-wind induced structural loads.

Yago and Endo (1996) and Hamamoto and Fujita (2002) studied hydroelastic responses of a freely floating rectangular barge and reported its vertical displacements under several incoming wave directions and periods. The prototype of these

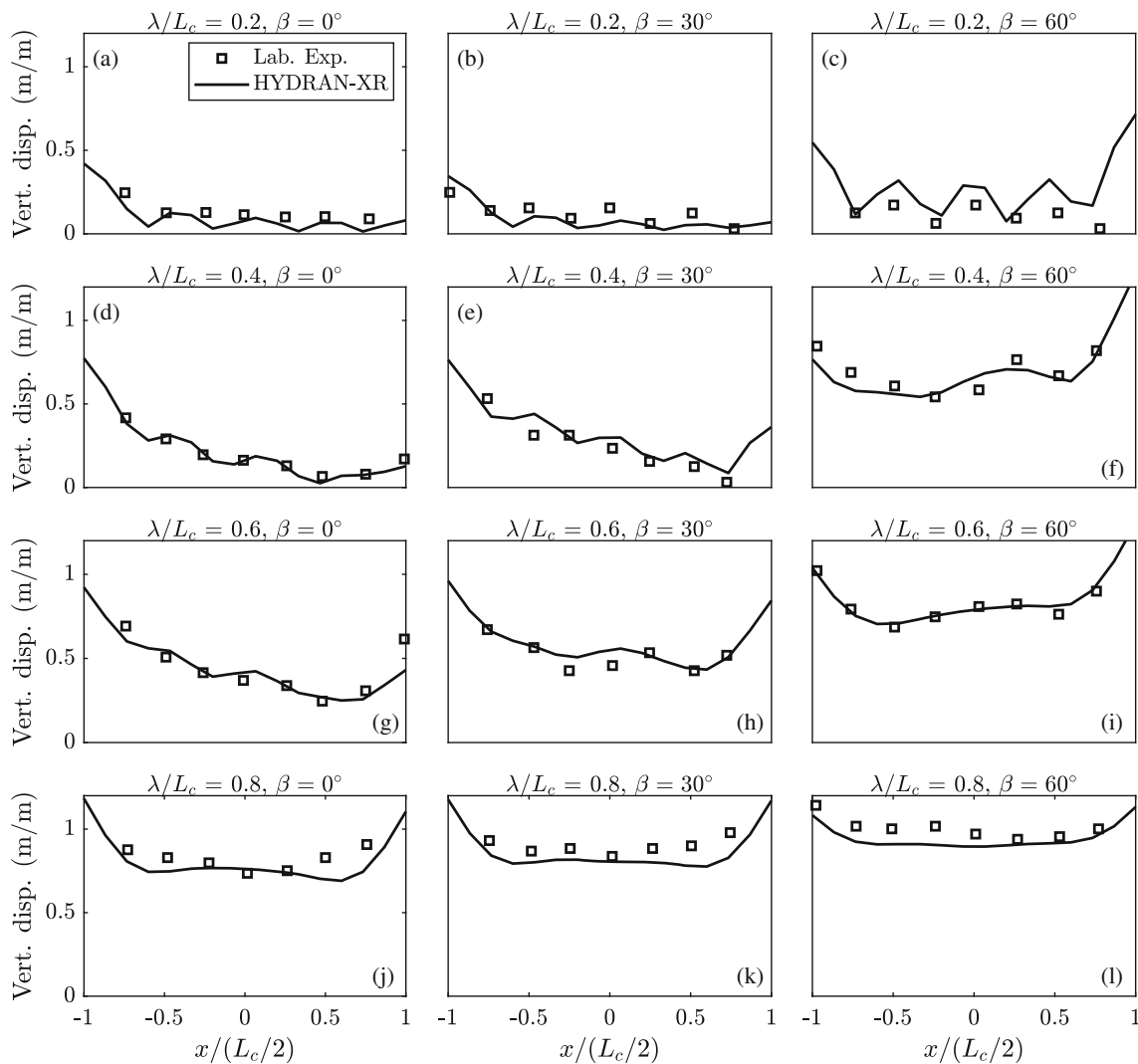


Fig. 9 Comparison of the vertical displacement along the centreline of the flexible barge computed by HYDRAN-XR and laboratory measurements of Yago and Endo (1996)

experiments is a steel barge, with an overall length of $L_c = 300$ m long, 60 m wide, and 2 m deep with a draft of 0.5 m. The laboratory experiments were carried out for a model with a scaling ratio of 1:30. In the experiments, the total mass of the scaled barge is 327 kg, with 683.8×10^2 MPa elasticity modulus and 0.3 Poisson's ratio. The density of the top and bottom plates of the barge is 315.6 kg/m^3 , with 0.02725 m shell thickness. The density of the side plates is assumed to be negligible.

The wave-induced vertical displacements of the barge along its horizontal centreline are computed by HYDRAN-XR and compared with the laboratory experiments. The computations for the panel size 0.325 m, 1010 wet panels, and for 5 wave frequencies required less than a minute. The mode-shapes of the barge are computed such that similar to a free-free beam, both ends of the barge are free. Figure 8 presents the first two generalized modes of the barge, the 7th

and 8th mode shapes. Figure 9 shows the distribution of the vertical displacements normalised by wave amplitude along the centreline of the barge and their comparison with the laboratory measurements in wave heading angles $\beta = 0^\circ$, $\beta = 30^\circ$ and $\beta = 60^\circ$. The results in Fig. 9 are presented as a function of the ratio between the wavelength, λ , and the length of the barge, L_c .

A non-uniform distribution of the vertical displacement along the barge length is observed. The vertical displacement increases gradually from the barge fore to the aft. The average displacement along the centreline of the barge increases with the wavelength, while the wavy distribution of the vertical displacement becomes flattened. This behaviour can be explained by the mode shapes of the flexible barge, the length and its material properties, and the incoming wave periods. As the incoming wave directions vary from head seas, the vertical displacement is increased slightly.

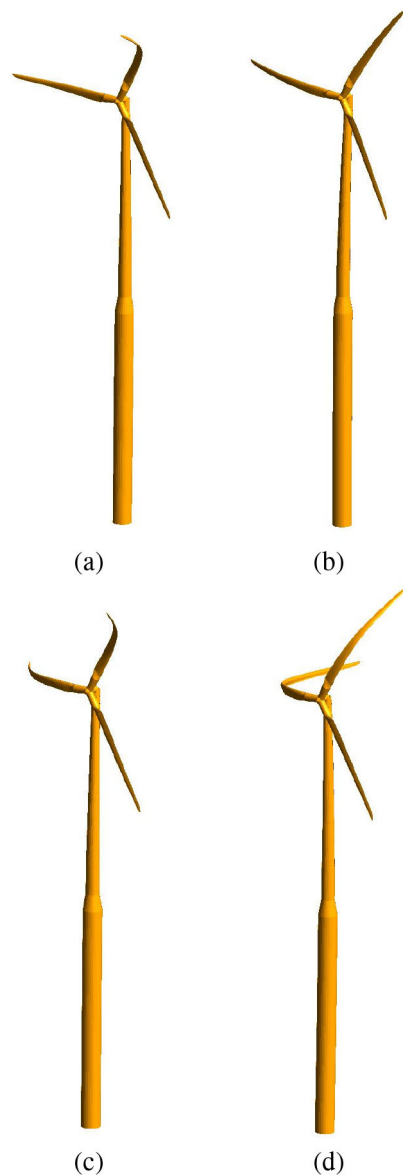


Fig. 10 The **a** 7th, **b** 8th, **c** 9th and **d** 10th mode-shapes of the flexible FOWT at its wet natural periods of $T_n = 2.219$ s, $T_n = 2.041$ s, $T_n = 1.965$ s and $T_n = 1.8661$ s (enlarged by a factor of 500)

Shown in Fig. 9, in spite of some small differences for wave heading angle 60° and λ/L_c at 0.2 and 0.8, see Fig. 10c, l, there is an excellent agreement between the results of HYDRAN-XR and the laboratory measurements.

Next, a fully flexible FOWT is modelled and its hydro- and aeroelastic responses are presented and discussed. There have been several FOWT concepts, but only a hand-full of these concepts have accessible structural details such as the OC3 SPAR FOWT. Although the substructure of the OC3 SPAR FOWT is designed to be rigid, this paper will also consider the hydroelastic responses of the structure. The finite element analysis tool of HYDRAN-XR is assessed in this

study and results are compared with laboratory measurements of the rigid OC3 SPAR FOWT.

The finite element model of the rotor and the tower of the OC3 SPAR FOWT is according to the system definition given by Jonkman et al. (2009). The material properties of the blades vary along their chords and their radius. A simplified model of the blades is used for this study. In this model, the blades are divided into 17 sections along their radius and the material properties are averaged over the chord at each section. The mass of the RNA is added at the top of the tower with nodal masses. As specified by Jonkman et al. (2009), the tower for the 5 MW NREL wind turbine is conical with decreasing diameter from bottom to top. The tower is modelled with three cylindrical segments, each with a uniform diameter along its length. The wall thicknesses of the cylindrical segments decreases linearly from 0.0351 m at the bottom to 0.0247 m at the top.

For the floating SPAR substructure, other than the geometrical dimensions, the details about its material properties, wall thickness, the mass distribution of the platform and the ballast weight were not reported. To model the SPAR platform, Leimeister et al. (2020) for instance, divided the platform in four cylindrical sections, where the bottom section was used for the ballast. Here, it is assumed that the SPAR platform is a continuation of the tower, with the same material properties. The wall thickness of the entire platform is assumed to be constant and equal to the wall thickness at the bottom of the tower, 0.0351 m.

The total mass of the ballast and its location is specified such that the total mass of the structure, the centre of gravity and the inertia moments match the values reported for the reference OC3 SPAR FOWT. With the specified material density and the wall thickness for the SPAR platform, the total mass of the added ballast is 6.6330×10^6 kg. It is assumed that the ballast inside the platform covers the bottom of the structure up to a specific height to result in the centre of gravity and the inertia moments given by the definition of the SPAR FOWT system. Similar to the RNA of the FOWT, the ballast is added to the platform with nodal masses. With an iterative procedure, the length of the bottom section of the platform, where the ballast nodal masses are assigned, is changed until the centre of gravity and inertia moments match their target values. The wall thicknesses of the tower and platform and the height of the ballast mass are reported in Table 2. In Table 3, the mass distribution of the SPAR FOWT finite element model in HYDRAN-XR is given. Furthermore, the additional viscous damping coefficients and the mooring stiffness specified by Jonkman et al. (2009) are implemented for the hydroelastic analysis of the SPAR FOWT.

Generalised modes of the flexible SPAR FOWT are determined by a finite element method. The equation of motion of the FOWT to combined wave and wind loads is solved for

Table 2 Structural properties of the tower and the platform of the flexible SPAR FOWT

Tower	
Top section, wall thickness (m)	0.0247
Middle section, wall thickness (m)	0.0299
Bottom section, wall thickness (m)	0.0351
Platform	
Wall thickness (m)	0.0351
Length of the ballast mass from the bottom of the platform (m)	49

Table 3 Mass distribution of the flexible SPAR FOWT model in HYDRAN-XR

Total mass (kg)	8.0660×10^6
Ballast mass (kg)	6.6330×10^6
Center of gravity (CG) below SWL (m)	77.0981
Roll inertia about CG (kg m^2)	2.2130×10^{10}
Pitch inertia about CG (kg m^2)	2.2116×10^{10}
Yaw inertia about CG (kg m^2)	1.7912×10^8

18 modes, i.e. six translational and rotational modes of the structure and 12 generalised modes, representing the flexibility of the structure. The wet mode-shapes of the flexible SPAR FOWT are computed, and the first four generalized modes are presented in Fig. 10. The first four mode-shapes are mainly dominated by the deflection of the blades of the 5 MW NREL wind turbine, and the contribution of the tower and the platform to the mode-shapes are negligible. This is

expected as the blades are more flexible than any other part of the SPAR FOWT.

The normalized added mass and damping coefficients for the first four generalized modes and their couplings with surge and pitch are presented in Fig. 11. As explained in Sect. 3, the generalized mode shapes and so the diagonal added mass and hydrodynamic damping coefficients are normalized by the mass of the structure. For comparison, the coupling components of the generalized modes with surge and pitch are normalized with the mass of the structure and the pitch rotational inertia, respectively. As shown in Fig. 11, the diagonal values of both added mass and hydrodynamic damping coefficients for modes 7, 8, and 9 are significantly smaller than in mode 10. Shown in Fig. 11c, the added mass coefficients coupling modes 7 and 9 with surge are approximately comparable in their magnitude. The same behaviour in Fig. 11d–f, between the coupling components of modes 7 and 9 with surge and pitch, i.e. B_{17} and B_{19} , A_{57} and

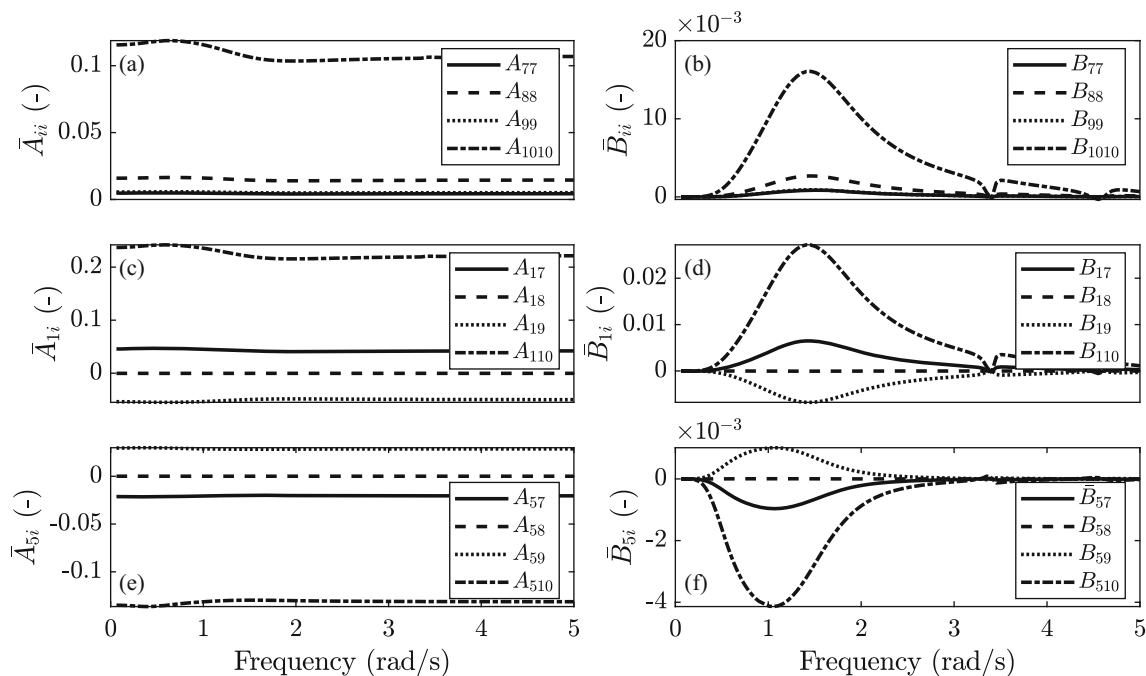


Fig. 11 Comparison of the normalized added mass and hydrodynamic damping coefficients of the fully flexible SPAR FOWT for the first four generalized modes, $i = 7, 8, 9$ and 10 and their coupling with surge, heave and pitch modes computed by HYDRAN-XR

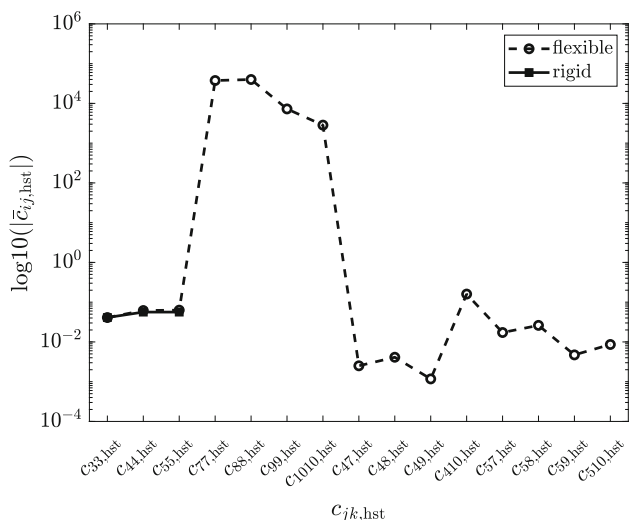


Fig. 12 Normalized hydrostatic restoring coefficients of the rigid and flexible SPAR FOWT for heave, roll and pitch and the first four generalized modes

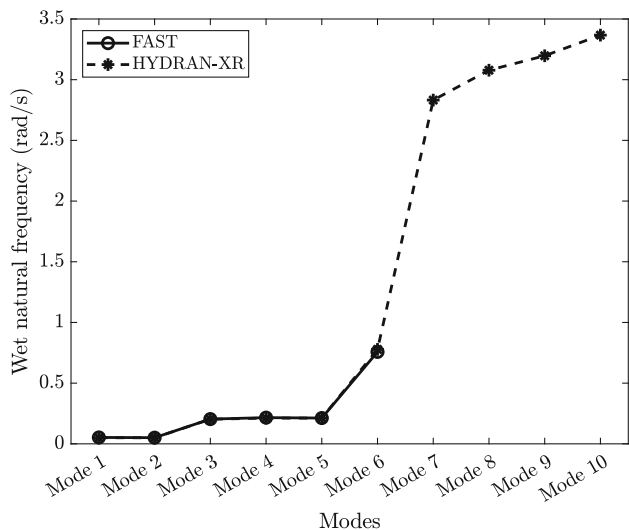


Fig. 13 Comparison of wet natural frequencies of the moored fully flexible SPAR FOWT computed by HYDRAN-XR and reported by FAST (Jonkman and Musial 2010)

A_{59} , B_{57} and B_{59} is observed. However, the coupling effects of the 8th and the 10th modes are the least and the highest with surge and pitch rigid body modes, among others. Similarly, Mantadakis et al. (2019) carried out a hydroelastic analysis of the fully flexible SPAR FOWT and presented its frequency-dependent coefficients for the first four generalized modes. However, the reported wet natural frequencies and consequently the added mass and damping coefficients are far different from the computations presented here. This difference is explained by normalization of the added mass and damping coefficients in the added generalized modes.

Shown in Fig. 12, the magnitude of the restoring coefficients of the rigid SPAR FOWT in its heave, roll and pitch

and for the first 10 modes of the flexible SPAR FOWT are presented. For comparison, the hydrostatic restoring coefficients are calculated for mass-normalized mode shapes. In Fig. 12, only the nonzero restoring coefficients in the generalized modes are shown. As explained in Sect. 4, the restoring coefficients are computed by Eq. (16), including the effects of both external forces and internal stresses of the structure. The normalized restoring coefficients in heave, roll and pitch are comparable with their counterparts for the rigid structure and considerably smaller than hydrostatic coefficients at modes 7, 8, 9 and 10. However, hydrostatic coefficients for the coupling effect of the generalized modes and roll and pitch have lower values compared with the rest of the presented restoring coefficients.

The wet natural frequencies of the full structure for the first 10 modes are presented in Fig. 13. The computed values in HYDRAN-XR for the six rigid modes are compared with their reported counterparts by Jonkman and Musial (2010). A close agreement between the natural frequencies determined by HYDRAN-XR and those reported by Jonkman and Musial (2010) are seen for the rigid body modes. As shown in Fig. 13, the natural frequencies in the generalized modes are in an interval of high wave frequencies, and less likely to be excited.

For a flexible structure, the equation of motion is solved for the total number of rigid-body and the added generalized modes. Due to the coupling effect of the generalized modes, the responses of the structure in its translational and rotational degrees of freedom might be different. The RAOs of the rigid and flexible SPAR FOWT in surge, heave and pitch obtained by HYDRAN-XR are presented in Fig. 14. For comparison, the numerical results of the flexible SPAR FOWT reported by Mantadakis et al. (2019) and the laboratory measurements of the rigid scaled model of Ahn and Shin (2017) are also included in Fig. 14. The peaks in surge and pitch RAOs computed by Mantadakis et al. (2019) are shifted to larger wave frequencies compared with the laboratory measurements and the numerical results for both rigid and flexible structures by HYDRAN-XR. The difference between the numerical RAOs of the flexible structure by HYDRAN-XR and Mantadakis et al. (2019) is more pronounced at the peak in heave at approximately $\omega = 0.2$ rad/s. Moreover, comparing the RAOs of the rigid and flexible FOWTs by HYDRAN-XR, by including the flexibility effects of the entire structure, peaks in both surge and pitch RAOs become smaller.

Next, we investigate the shear forces and moments on a cross-section of the platform at the SWL. The stresses on each element of the circular cross-section are determined at each quadrant based on the local coordinate system of the quadrant, shown in Fig. 15. The forces and moments are then transferred from the local coordinate system of the elements to the global coordinate system of the structure, shown in Fig. 15. Based on the direction of the local coordinate sys-

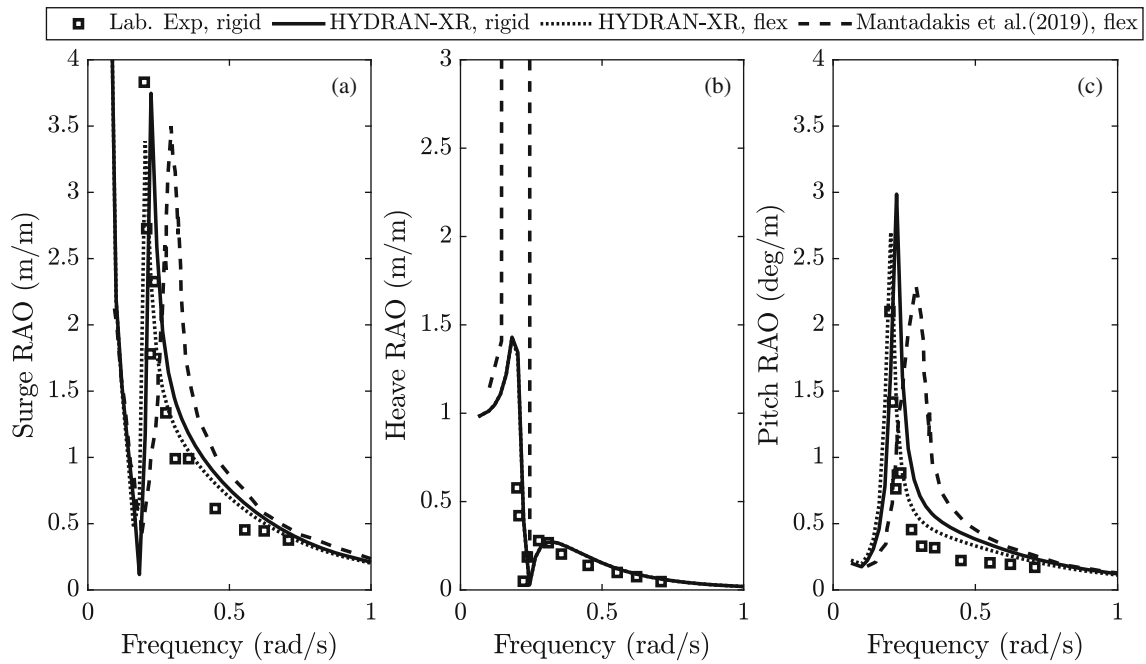


Fig. 14 Comparison of the wave-induced RAOs of fully flexible SPAR FOWT by HYDRAN-XR with laboratory measurements of Ahn and Shin (2017) and numerical results by Mantadakis et al. (2019)

Fig. 15 Top view of the global coordinate system at a cross section of the platform at the SWL and the local coordinate systems of the elements at the cross section. The local coordinate system of the elements in each quadrant of the cross section are the same. Numbers refer to the order of elements. Circles with a dot and a cross describe the direction of the vector out of and into the paper, respectively

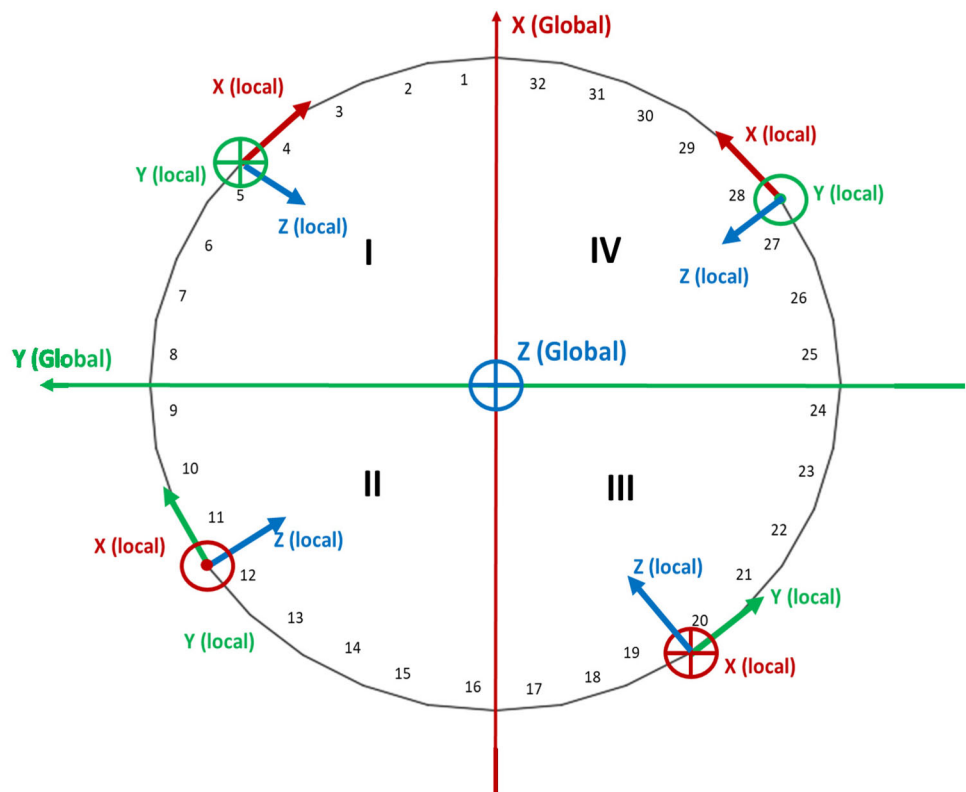
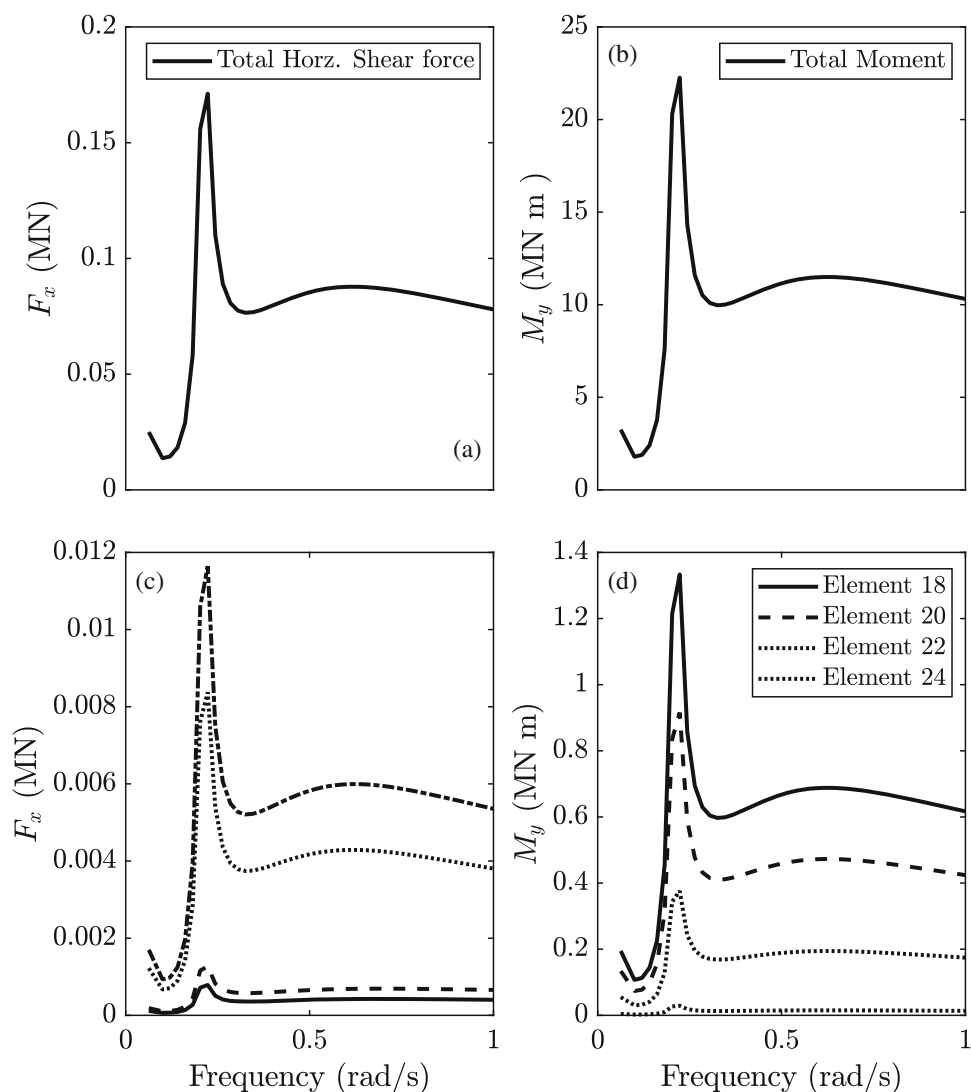


Fig. 16 The wave-induced **a** total horizontal shear force at the SWL on the platform, **b** total moment about the y -axis at the SWL on the platform, **c** contribution to the horizontal shear force by Elements 18, 20, 22 and 24, and **d** contribution to the moment about the y -axis by Elements 18, 20, 22 and 24



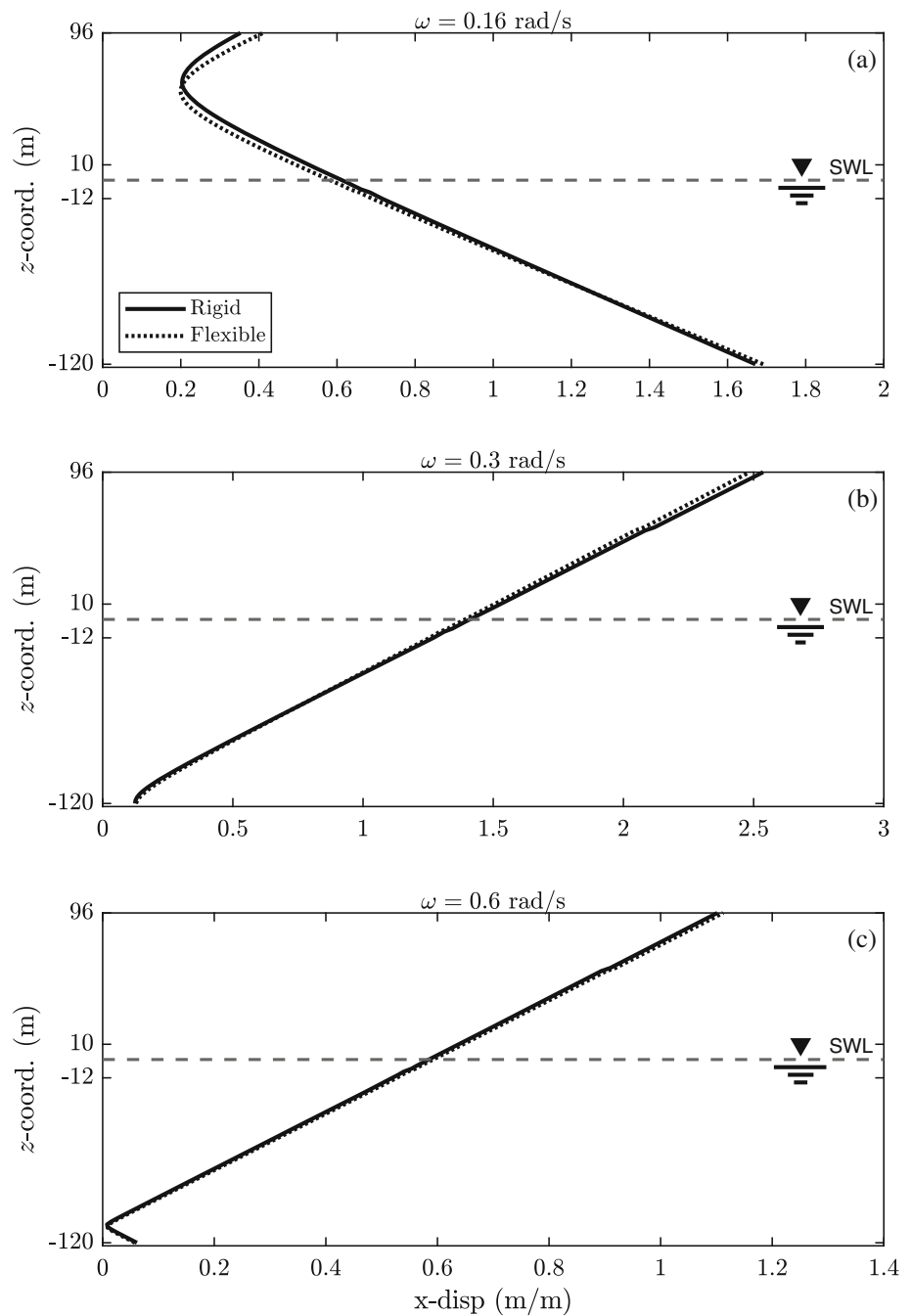
tem, in-plane tensile stress resultants either in local x - or y -direction contribute to the global moments about x - and y -axis. The local bending moment of each element is negligible and it is not accounted in element contribution to the total moment about global x - and y -axis. Furthermore, the in-plane and transverse shear stress resultants of each element contribute to the total shear forces in the global coordinate system. There are 32 elements at the perimeter of the cross section, shown in Fig. 15, and the local coordinate system of the elements in each quadrant is the same.

Figure 16 presents the total shear force, F_x , and moment, M_y on the cross-section of the structure. Also included in Fig. 16 is the contribution of the shear force and the moment by elements, on sample points of the cross-section (here, Elements 18, 20, 22 and 24 in Quadrant III are considered). Similar peaks are observed at the same frequency $\omega = 0.2 \text{ rad/s}$ approximately the natural frequency of the pitch and heave of the SPAR FOWT, in both the total force

and moment and for the element contributions. Among the four elements, Element 18 with the largest arm with respect to the global y -axis has the highest contribution to the bending moment about y -axis, compared with Elements 20, 22 and 24. Moreover, in Quadrant III, the angle between the global x -axis and the local Y -axis on Element 24 is the smallest compared with other three elements, resulting in the largest contribution to the horizontal shear force of Element 24 in comparison with Elements 18, 20 and 22.

Figure 17 compares the maximum wave-induced horizontal nodal displacements of the fully flexible SPAR FOWT with its rigid counterparts. For the rigid FOWT, the horizontal displacements along the structure are the sum of the motion of the structure in surge and the displacements due to the rotation of the structure about the y -axis. Regarding the fully flexible FOWT, in addition to the motions of the structure in its rigid body degrees of freedom, the displacements due to the flexibility effects of the FOWT contribute to

Fig. 17 Comparison of the horizontal wave-induced nodal displacements of the rigid and fully flexible SPAR FOWTs computed by HYDRAN-XR



the total horizontal displacement of the structure. The nodal displacements presented in Fig. 17 are the magnitude of the maximum displacements of a node on the structure. The maximum displacements of the nodes may not occur at the same time, hence, the displacements of the rigid body do not follow a straight line.

The displacements are shown for three wave frequencies, one before the peak in surge RAOs ($\omega = 0.16$ rad/s) and two wave frequencies larger than 0.2231 rad/s, i.e. $\omega = 0.3$ rad/s and 0.6 rad/s. In Fig. 17, on the y -axis, three key vertical locations along the platform and the tower are specified. The

horizontal dashed line represents the SWL, the substructure cross section is tapered to a smaller diameter at $z = -12$ m, and the tower starts at 10 m above the free surface. The horizontal displacements are computed for 109 nodes from the bottom of the SPAR platform up to the top of the tower. The nodes are located at the leading edge of the structure, facing the incoming waves. The displacements of the structure in x -direction start from small values for ω lower than the peak frequency. Similar to the surge RAOs, for $\omega > 0.2231$ rad/s, the magnitude of the displacements decrease.

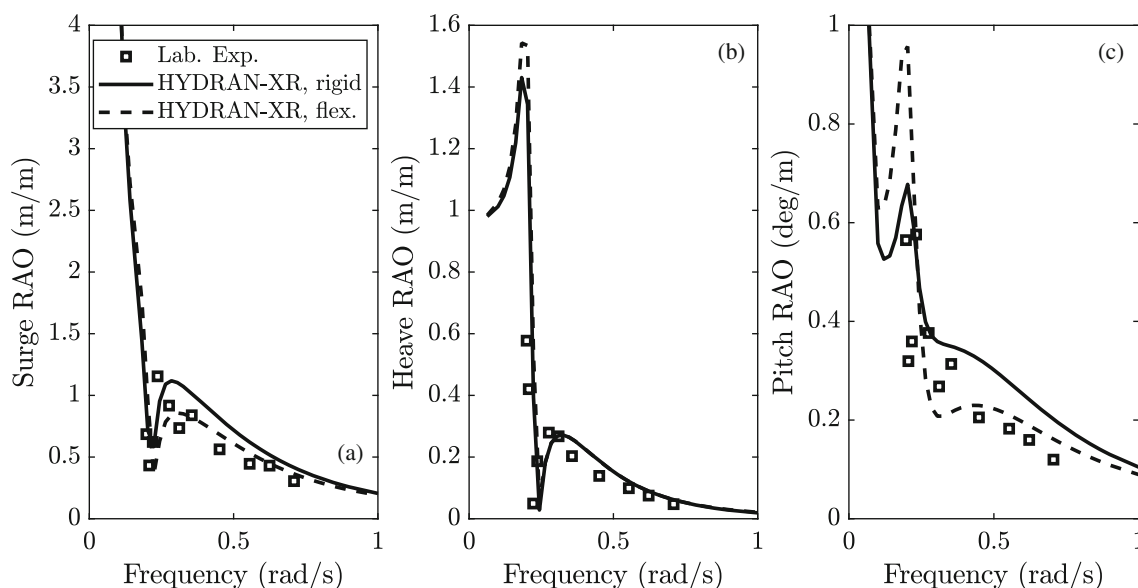


Fig. 18 Comparison of the wind- and wave-induced RAOs of rigid and flexible SPAR FOWT by HYDRAN-XR with laboratory measurements of Ahn and Shin (2017)

At $\omega = 0.16 \text{ rad/s}$, although the tower top of the rigid FOWT experiences slightly smaller horizontal displacements than the flexible FOWT, the displacements along the platforms of both rigid and flexible structures are the same. As the wave frequency increases, the tower top undergoes a larger displacement than the rest of the nodes along the structure. At $\omega = 0.3 \text{ rad/s}$ and $\omega = 0.6 \text{ rad/s}$ cases, the horizontal displacements of the rigid and flexible structures are almost identical. Also seen in Fig. 17, at $\omega = 0.16 \text{ rad/s}$ and $\omega = 0.6 \text{ rad/s}$, the minimum nodal displacements are observed at approximately $z = 60 \text{ m}$ and $z = -110 \text{ m}$, respectively. The minimum horizontal displacement corresponds to the centre of pitch rotation of the SPAR at a given wave frequency. See Kaptan et al. (2022) for a discussion on the change of centre of rotation of a SPAR FOWT in different wave frequencies.

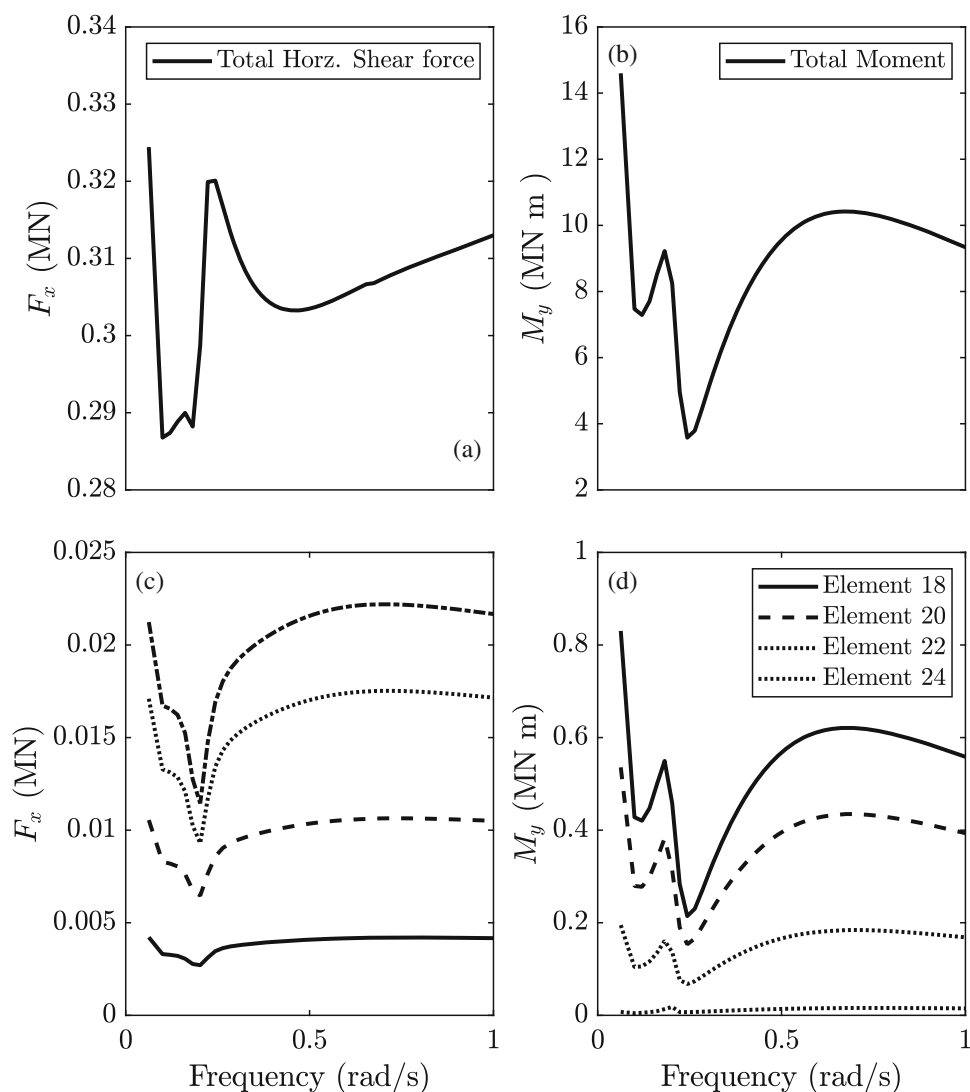
Next, the responses of the fully flexible structure are computed for regular waves and steady wind at 11.4 m/s . The rigid body responses of the SPAR FOWT to combined wind and wave loads were obtained in Sect. 2. Figure 18 shows the comparison of the RAOs computed in HYDRAN-XR for the fully flexible and the rigid SPAR FOWTs, and the laboratory measurements of Ahn and Shin (2017) for the rigid structure. The elasticity effects of the FOWT have resulted in some changes in its responses over the wave frequencies. As shown in Fig. 18, the flexibility of the structure causes a slight decrease in surge RAOs for approximately $\omega > 0.25 \text{ rad/s}$. For the same interval of the wave frequencies, the pitch RAOs of the flexible FOWT decrease compared with the rigid structure. Furthermore, the peak in pitch RAOs at approximately $\omega = 0.2 \text{ rad/s}$ is 0.3 deg/m larger than the peak computed for

the rigid FOWT. The elasticity effect of the structure on its heave RAOs are negligible and the heave responses for both rigid and flexible FOWTs are almost identical.

The total wave- and wind-induced horizontal shear force and moment about the y -axis on the cross-section of the structure and the contribution of four Elements 18, 20, 22 and 24 to F_x and M_y in Quadrant III (shown in Fig. 15) are presented in Fig. 19. Both the shear forces and moments experience a sharp drop at approximately $\omega = 0.2 \text{ rad/s}$. The total and contribution of elements in shear forces gradually become steady after approximately $\omega = 0.6 \text{ rad/s}$. Similar to Fig. 16, Element 18 experiences the largest moment contribution about the y -axis compared with Elements 20, 22 and 24. Comparing the shear forces and moments due to wave loads (shown in Fig. 16) with those due to combined wave and wind loads (given in Fig. 19), we observe larger horizontal shear forces (about three times larger) and smaller moments about the y -axis on the same elements due to the addition of aerodynamic excitation forces and aerodynamic damping effect, respectively. Similarly, including the aerodynamic loads results in increase and decrease of the total horizontal shear force and the total moment about the y -axis, respectively compared with its wave-induced counterparts.

The maximum nodal displacement of the structure under combined wind and wave loads are computed in x -directions, shown in Fig. 20. For this purpose, similar to the hydroelastic analysis, 109 nodes over the front side of the platform and the tower, at the furthest distance from the x -axis are chosen. The nodal displacements for $\omega = 0.16 \text{ rad/s}$ are significantly larger than the displacements presented for the other two wave frequencies. This is because, as it is shown

Fig. 19 The **a** total horizontal shear force at the SWL on the platform, **b** total moment about the y -axis at the SWL on the platform, **c** contribution to the horizontal shear force by Elements 18, 20, 22 and 24, and **d** contribution to the moment about the y -axis by Elements 18, 20, 22 and 24 by combined wind and wave loads



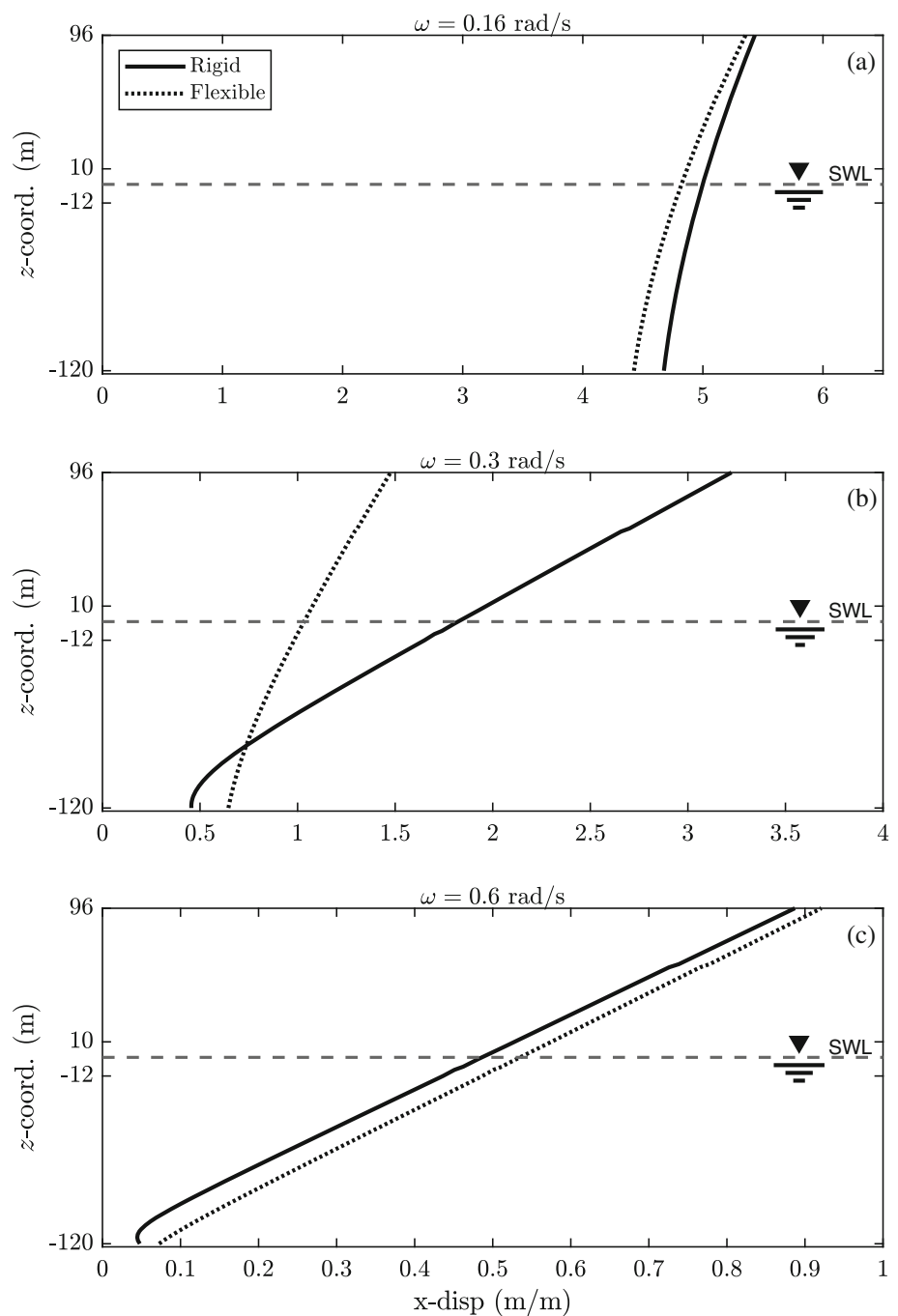
in Fig. 18, the surge RAOs at $\omega = 0.16$ rad/s are larger than those at $\omega = 0.3$ rad/s and 0.6 rad/s. For the displacements in x -direction, the difference between the rigid and the flexible structures is the largest at $\omega = 0.3$ rad/s among the three wave frequencies, due to the large difference between the rigid- and flexible-body surge and pitch RAOs at $\omega = 0.3$ rad/s, see Figs. 7 and 18. Moreover, shown in Fig. 20b, the horizontal displacement of the nodes above the SWL show that the flexibility effects of the tower on the deflection of the structure is more pronounced than the hydroelasticity effects of the platform. At $\omega = 0.3$ rad/s and $\omega = 0.6$ rad/s, the minimum horizontal nodal displacements occur at approximately $z = -110$ m, which is the center of the pitch rotation of the SPAR FOWT at these frequencies.

7 Concluding remarks

An analytical approach and numerical solution are developed to determine the motion and elastic responses of FOWTs to combined wave and wind loads. The elasticity of the entire FOWT is considered and its elastic motions to aerodynamic and hydrodynamic loads are obtained. The model, an enhanced version of HYDRAN-XR, consists of three integrated modules for structural, aerodynamic and hydrodynamic analysis.

With the finite element method, the mode-shapes of the complete structure are prescribed and are added as generalized modes to the six rigid-body degrees of freedom. The aerodynamic analysis includes the loads on both the rotor

Fig. 20 Comparison of the horizontal nodal displacements of the rigid and fully flexible SPAR FOWTs to combined wind and wave loads computed by HYDRAN-XR



and the tower of the turbine. The aerodynamic load on the rotor is computed with the steady BEM method, and is distributed along the blades rather than adding the integrated aerodynamic normal force at the hub centre. The hydrodynamic analysis of the floating structure is accomplished by use of the linear boundary element method.

In this approach, the system of equations of floating offshore wind turbines is solved in frequency domain. In our formulation, wind may have arbitrary speed and consequently there is no restriction on the wind load magnitude

(which is proportional to the square of the wind speed). Comparison of the results of the model with available laboratory experiments for combined wave and wind load on structures show very good agreement for this frequency-domain analysis. Time-domain analysis would be required if nonlinear effects are to be considered.

The coupled fluid-structural dynamics is solved with a finite element model that conforms to the panel mesh for hydrodynamic analysis with a one-to-one mapping. Therefore, the finite element model of the structure uses shell

elements. It is shown that the simulation time in frequency domain analysis of the FOWTs is remarkably smaller than existing coupling approaches in the time-domain, making this model very attractive for the concept and design stages of FOWTs.

HYDRAN-XR is used to determine the wave-induced, and combined wave- and wind-induced responses of a SPAR FOWT and results are compared with the laboratory measurements. A direct comparison of the responses of a FOWT to wave, and combined wind and wave loads show that the elasticity of the floating structure (often not considered thus far) can play a remarkable role in the responses (and hence performance) of the FOWT. Due to the addition of elasticity effects of the entire structure, deviations were observed in the computed RAOs for the fully flexible FOWT compared with its rigid body motions. As a result, the flexibility of the structure may influence the responses of the structure significantly and has to be considered for its loads and motions analyses. Moreover, the hydroelastic analysis allows for determination of the structural loads and deformations.

Offshore wind energy, and the involved engineering and scientific challenges are rapidly emerging and new concepts are introduced. This study shows that HYDRAN-XR can be used to determine the loads, motions, and elastic responses of floating objects of arbitrary shape to combined wind and wave loads in any water depth.

Acknowledgements The work of AL and MH is partially based on funding from the CBJ Ocean Engineering Corp. of Hong Kong. This funding is gratefully acknowledged. Any findings and opinions contained in this paper are those of the authors and do not necessarily reflect the opinions of the funding company. Shuijin Li of the University of Dundee has assisted in performing some of the FAST computations, and this is much appreciated.

Data availability The data that support the findings of this study are available within the article.

Open Access This article is licensed under a Creative Commons Attribution 4.0 International License, which permits use, sharing, adaptation, distribution and reproduction in any medium or format, as long as you give appropriate credit to the original author(s) and the source, provide a link to the Creative Commons licence, and indicate if changes were made. The images or other third party material in this article are included in the article's Creative Commons licence, unless indicated otherwise in a credit line to the material. If material is not included in the article's Creative Commons licence and your intended use is not permitted by statutory regulation or exceeds the permitted use, you will need to obtain permission directly from the copyright holder. To view a copy of this licence, visit <http://creativecommons.org/licenses/by/4.0/>.

References

- Ahn HJ, Shin H (2017) Model test and numerical simulation of OC3 SPAR type floating offshore wind turbine. *Int J Nav Archit Ocean Eng* 11:1–10. <https://doi.org/10.1016/j.ijnaoe.2017.09.010>
- Bae YH, Kim MH (2014) Coupled dynamic analysis of multiple wind turbines on a large single floater. *Ocean Eng* 92:175–187. <https://doi.org/10.1016/j.oceaneng.2014.10.001>
- Bae YH, Kim MH (2015) The dynamic coupling effects of a MUFOWT (multiple unit floating offshore wind turbine) with partially broken blade. *J Ocean Wind Energy* 2:89–97
- Bashetty S, Ozcelik S (2020a) Aero-hydrodynamic analysis of an offshore floating multi-wind-turbine platform—part I. In: 2020 IEEE 3rd international conference on renewable energy and power engineering (REPE), October 9–11. Edmonton, Canada. IEEE, pp 1–6
- Bashetty S, Ozcelik S (2020b) Aero-hydrodynamic analysis of an offshore floating multi-wind-turbine platform—part II. In: 2020 IEEE 3rd international conference on renewable energy and power, October 9–11. Edmonton, Canada, pp 1–6
- Bashetty S, Ozcelik S (2020c) Design and stability analysis of an offshore floating multi-turbine platform. In: 2020 IEEE green technologies conference (GreenTech), April 1–3. Oklahoma, USA, pp 1–6
- Bishop RED, Price WG, Wu Y (1986) A general linear hydroelasticity theory of floating structures moving in a seaway. *Philos Trans R Soc A Math Phys Eng Sci* 316:375–426. <https://doi.org/10.1098/rsta.1986.0016>
- Borg M, Bredmose H, Hansen AM, (2017). Elastic deformations of floaters for offshore wind turbines: Dynamic modelling and sectional load calculations. In: Proceedings of the 36th international conference on offshore mechanics and arctic engineering—OMAE, ASME, June 25–30, Trondheim, Norway, pp 1–10. <https://doi.org/10.1115/OMAE2017-61446>
- Bruinsma N, Paulsen BT, Jacobsen NG (2018) Validation and application of a fully nonlinear numerical wave tank for simulating floating offshore wind turbines. *Ocean Eng* 147:647–658. <https://doi.org/10.1016/j.oceaneng.2017.09.054>
- Chen J, Hu Z, Liu G, Wan D (2019) Coupled aero-hydro-servo-elastic methods for floating wind turbines. *Renew Energy* 130:139–153. <https://doi.org/10.1016/j.renene.2018.06.060>
- Chen JH, Guo Pei A, Chen P, Qiang Hu Z (2021) Study on gyroscopic effect of floating offshore wind turbines. *China Ocean Eng* 35:201–214. <https://doi.org/10.1007/s13344-021-0018-z>
- Chen Y, Zhou S, Cai C, Wang W, Hao Y, Zhou T, Wang X, Li Q (2023) Study on the rotation effect on the modal performance of wind turbine blades. *Energies* 16:1–11. <https://doi.org/10.3390/en16031036>
- Chuang TC, Yang WH, Yang RY (2021) Experimental and numerical study of a barge-type FOWT platform under wind and wave load. *Ocean Eng* 230:1–24. <https://doi.org/10.1016/j.oceaneng.2021.109015>
- Coulling AJ, Goupee AJ, Robertson AN, Jonkman JM, Dagher HJ (2013) Validation of a FAST semisubmersible floating wind turbine numerical model with deep wind test data. *J Renew Sustain Energy* 5:1–29. <https://doi.org/10.1063/1.4796197>
- Cruz J, Atcheson M (eds) (2016) Floating offshore wind energy. In: Green energy and technology. Springer International Publishing, Lisbon. <https://doi.org/10.1007/978-3-319-29398-1>
- Ertekin RC, Riggs HR, Che XL, Du SX (1993) Efficient methods for hydroelastic analysis of very large floating structures. *J Ship Res* 37:58–76. <https://doi.org/10.5957/jsr.1993.37.1.58>
- Govindji AK, James R, Carvallo A (2014) Appraisal of the offshore wind industry in Japan. Technical Report. CarbonTrust, British Embassy, Tokyo. Accessed Dec 2020
- Hamamoto T, Fujita K (2002) Wet-mode superposition for evaluating the hydroelastic response of floating structures with arbitrary shape. In: Proceedings of the 12th international offshore and polar engineering conference. The International Society of Offshore and Polar Engineers, May 26–31, Kitakyushu, Japan, pp 290–297
- Hansen MOL (2007) Aerodynamics of wind turbines, 2nd edn. Earthscan Publications Ltd, London

- Hansen MOL, Sørensen JN, Voutsinas S, Sørensen N, Madsen HA (2006) State of the art in wind turbine aerodynamics and aeroelasticity. *Prog Aerosp Sci* 42:285–330. <https://doi.org/10.1016/j.paerosci.2006.10.002>
- Hanssen JE, Margheritini L, O’Sullivan K, Mayorga P, Martinez I, Arriaga A, Agos I, Steynor J, Ingram D, Hezari R, Todalshaug JH (2015) Design and performance validation of a hybrid offshore renewable energy platform. In: 2015 Tenth international conference on ecological vehicles and renewable energies (EVER), March 31–April 2, Monte-Carlo, Monaco. IEEE, pp 1–8. <https://doi.org/10.1109/EVER.2015.7113017>
- Hegseth JM, Bachynski EE, Karimirad M (2018) Comparison and validation of hydrodynamic load models for a semisubmersible floating wind turbine. In: Proceedings of the 37th international conference on offshore mechanics and arctic engineering—OMAE, ASME, June 17–22, Madrid, Spain, pp 1–11. <https://doi.org/10.1115/OMAE2018-77676>
- Høeg CE, Zhang Z (2021) The influence of gyroscopic effects on dynamic responses of floating offshore wind turbines in idling and operational conditions. *Ocean Eng* 227:1–29. <https://doi.org/10.1016/j.oceaneng.2021.108712>
- Hoerner SF (1958) Fluid-dynamic drag: practical information on aerodynamic drag and hydrodynamic resistance, 2nd edn. Hoerner Fluid Dynamics, Bakersfield, CA, pp 1–460
- Hu C, Sueyoshi M, Liu C, Liu Y (2014) Hydrodynamic analysis of a semi-submersible-type floating wind turbine. *J Ocean Wind Energy* 1:202–208
- Huang LL, Riggs HR (2000) The hydrostatic stiffness of flexible floating structures for linear hydroelasticity. *Mar Struct* 13:91–106. [https://doi.org/10.1016/S0951-8339\(00\)00007-1](https://doi.org/10.1016/S0951-8339(00)00007-1)
- Ishihara T, Phuc PV, Sukegawa H (2007) A numerical study on the dynamic response of a floating offshore wind turbine system due to resonance and nonlinear wave. In: 2nd European offshore wind (EOW) conference, December 4–6, Berlin, Germany, pp 4–6
- Jang HK, Kim HC, Kim MH, Kim KH (2015) Coupled dynamic analysis for multi-unit floating offshore wind turbine in maximum operational and survival conditions. In: Proceedings of the 34th international conference on offshore mechanics and arctic engineering—OMAE, ASME, May 31–June 5, Newfoundland, Canada, pp 1–8. <https://doi.org/10.1115/OMAE2015-42062>
- Jonkman JM (2007) Dynamics modeling and loads analysis of an offshore floating wind turbine. PhD thesis, University of Colorado - Boulder
- Jonkman JM (2010) Definition of the floating system for phase IV of OC3. Accessed: December 2020. Technical Report. National Renewable Energy Laboratory (NREL/TP-500-47535). Golden, CO, USA. <https://doi.org/10.2172/979456>
- Jonkman J, Musial W (2010) Offshore Code Comparison Collaboration (OC3) for IEA Task 23 Offshore Wind Technology and Deployment Offshore Code Comparison Collaboration (OC3) for IEA Task 23 Offshore Wind Technology and Deployment. Technical Report December, National Renewable Energy Laboratory (NREL/TP-5000-48191)
- Jonkman JM, Butterfield S, Musial W, Scott G (2009) Definition of a 5-MW reference wind turbine for offshore system development. Accessed: December 2020. Technical Report. National Renewable Energy Laboratory (NREL/TP-500-38060). Golden, CO, USA. <https://doi.org/10.2172/947422>
- Jonkman JM, Wright AD, Hayman GJ, Robertson AN (2018) Full-system linearization for floating offshore wind turbines in OpenFAST. In: 1st international offshore wind technical conference, ASME, November 4–7, San Francisco, CA, USA, pp 1–10. <https://doi.org/10.1115/iowtc2018-1025>
- Jonkman JM, Damiani RR, Branlard ESP, Hall M, Robertson AN, Hayman GJ (2019) Substructure flexibility and member-level load capabilities for floating offshore wind turbines in OpenFAST. In: ASME 2019 2nd international offshore wind technical conference, ASME, November 3–9, St. Julian’s, Malta, pp 1–8. <https://doi.org/10.1115/IOWTC2019-7566>
- Jonkman JM, Branlard ESP, Hall M, Hayman GJ, Platt A, Robertson AN (2020) Implementation of substructure flexibility and member-level load capabilities for floating offshore wind turbines in OpenFAST. Technical Report August. National Renewable Energy Laboratory & Hayman Consulting, LLC
- Kang HY, Kim MH, Kim KH, Hong KY (2017) Hydroelastic analysis of multi-unit floating offshore wind turbine platform (MUFOWT). In: Proceedings of the 27th international offshore and polar engineering conference, ISOPE, June 25–30, San Francisco, CA, USA, pp 554–560
- Kaptan M, Skaare B, Jiang Z, Ong MC (2022) Analysis of spar and semi-submersible floating wind concepts with respect to human exposure to motion during maintenance operations. *Mar Struct* 83:1–20. <https://doi.org/10.1016/j.marstruc.2021.103145>
- Karimi M, Buckham B, Crawford C (2019) A fully coupled frequency domain model for floating offshore wind turbines. *J Ocean Eng Mar Energy* 5:135–158. <https://doi.org/10.1007/s40722-019-00134-x>
- Kim Y, Kwon OJ (2019) Effect of platform motion on aerodynamic performance and aeroelastic behavior of floating offshore wind turbine blades. *Energies* 12:1–24. <https://doi.org/10.3390/en12132519>
- Kvittem MI, Moan T (2014) Frequency versus time domain fatigue analysis of a semisubmersible wind turbine tower. *J Offshore Mech Arct Eng* 137:1–11. <https://doi.org/10.1115/1.4028340>
- Lamei A, Hayatdavoodi M, Wong C, Tang B (2019) On motion and hydroelastic analysis of a floating offshore wind turbine. In: Proceedings of the 38th international conference on offshore mechanics and arctic engineering—OMAE, ASME, June 9–14, Glasgow, UK, pp 1–10. <https://doi.org/10.1115/OMAE2019-96034>
- Lamei A, Hayatdavoodi M (2020) On motion analysis and elastic response of floating offshore wind turbines. *J Ocean Eng Mar Energy* 6:71–90. <https://doi.org/10.1007/s40722-019-00159-2>
- Lamei A, Hayatdavoodi M, Riggs HR (2022) Motion and elastic response of wind-tracing floating offshore wind turbines. *J Ocean Eng Mar Energy*. <https://doi.org/10.1007/s40722-022-00250-1>
- Lee J, Zhao F (2023) Global Wind Report 2023. Technical Report. Global Wind Energy Council, Brussels, Belgium
- Leimeister M, Kolios A, Collu M (2020) Development and verification of an aero-hydro-servo-elastic coupled model of dynamics for FOWT, based on the MoWIT library. *Energies* 13:1–33. <https://doi.org/10.3390/en13081974>
- Lemmer F, Yu W, Luhmann B, Schlipf D, Cheng PW (2020) Multibody modeling for concept-level floating offshore wind turbine design. *Multibody SysDyn* 49:203–236. <https://doi.org/10.1007/s11044-020-09729-x>
- Li L (2022) Full-coupled analysis of offshore floating wind turbine supported by very large floating structure with consideration of hydroelasticity. *Renew Energy* 189:790–799. <https://doi.org/10.1016/j.renene.2022.03.063>
- Liu Y, Xiao Q (2019) Development of a fully coupled aero-hydro-mooring-elastic tool for floating offshore wind turbines. *J Hydrodyn* 31:21–33. <https://doi.org/10.1007/s42241-019-0012-6>
- Liu Y, Xiao Q, Incecik A, Peyrard C, Wan D (2017) Establishing a fully coupled CFD analysis tool for floating offshore wind turbines. *Renew Energy* 112:280–301. <https://doi.org/10.1016/j.renene.2017.04.052>
- Lupton R (2014) Frequency-domain modelling of floating wind turbines. PhD thesis, University of Cambridge
- MacCamy R, Fuchs R (1954) Wave forces on piles: a diffraction theory. Tech. Memo. No. 69, Beach Erosion Board. Army Corps of Engineers, 1–17

- Mantadakis N, Loukogeorgaki E, Karimirad M (2019) Accounting for hydroelasticity in the analysis of offshore wind turbine SPAR-type platforms. In: Proceedings of the 29th international offshore and polar engineering conference, ISOPE, June 16–21, Honolulu, Hawaii, USA, pp 376–383
- Matha D, Schlipf M, Cordle A, Pereira R, Jonkman JM (2011) Challenges in simulation of aerodynamics, hydrodynamics, and mooring-line dynamics of floating offshore wind turbines. In: Proceedings of the 21th international offshore and polar engineering conference, ISOPE, June 19–24, Maui, Hawaii, USA, pp 421–428
- Newman JN (1994) Wave effects on deformable bodies. *Appl Ocean Res* 16:47–59. [https://doi.org/10.1016/0141-1187\(94\)90013-2](https://doi.org/10.1016/0141-1187(94)90013-2)
- NumSoft Technologies (2020) HYDRAN-XR, Hydrodynamic response analysis with integrated structural finite element analysis, version 20.1. Accessed: Dec 2020. Technical Report. Numsoft Technologies
- Pegalajar-Jurado A, Borg M, Bredmose H (2018) An efficient frequency-domain model for quick load analysis of floating offshore wind turbines. *Wind Energy Sci* 3:693–712. <https://doi.org/10.5194/wes-3-693-2018>
- Rodriguez SN, Jaworski JW (2020) Strongly-coupled aeroelastic free-vortex wake framework for floating offshore wind turbine rotors. part 2: application. *Renew Energy* 149:1018–1031. <https://doi.org/10.1016/j.renene.2019.10.094>
- Salehyar S, Li Y, Zhu Q (2017) Fully-coupled time-domain simulations of the response of a floating wind turbine to non-periodic disturbances. *Renew Energy* 111:214–226. <https://doi.org/10.1016/j.renene.2017.04.017>
- Uzunoglu E, Karmakar D, Guedes Soares C (2016) Floating offshore wind platforms. In: Castro-Santos L, Diaz-Casas V (eds) *Floating offshore wind platforms*, vol 1. Springer, Berlin, pp 53–77
- Wang D, Riggs HR, Ertekin RC (1991) Three-dimensional hydroelastic response of a very large floating structure. *Int J Offshore Polar Eng* 1:307–316
- Wang K, Ji C, Xue H, Tang W (2016) Frequency domain approach for the coupled analysis of floating wind turbine system. *Ships Offshore Struct* 5302:1–8. <https://doi.org/10.1080/17445302.2016.1241365>
- Wehausen JV, Laitone EV (1960) Surface waves. In: *Encyclopaedia of physics*, vol IX. Springer, pp 446–778. <https://doi.org/10.1515/9781400835676.225>
- Wu Y, Wang D, Riggs HR, Ertekin RC (1993) Composite singularity distribution method with application to hydroelasticity. *Mar Struct* 6:143–163. [https://doi.org/10.1016/0951-8339\(93\)90017-W](https://doi.org/10.1016/0951-8339(93)90017-W)
- Yago K, Endo H (1996) On the hydroelastic response of box-shaped floating structure with shallow draft. *J Soc Nav Archit Jpn* 180:341–352

Publisher's Note Springer Nature remains neutral with regard to jurisdictional claims in published maps and institutional affiliations.